Measurements and modeling of the interhemispheric differences of atmospheric chlorinated very short-lived substances

Behrooz Roozitalab[1], Louisa K. Emmons[1], Rebecca S. Hornbrook[1], Douglas E. Kinnison[1], Rafael P. Fernandez[2], Qinyi Li[2,3], Alfonso Saiz-Lopez[2], Ryan Hossaini[4], Carlos A. Cuevas[2], Alan J. Hills[1], Stephen A. Montzka[5], Donald R. Blake[6], William H. Brune[7], and Patrick R. Veres[8], and Eric C. Apel[1]

[1] Atmospheric Chemistry Observations & Modeling Laboratory, NSF National Center for Atmospheric Research, Boulder, CO, USA
[2] Department of Atmospheric Chemistry and Climate, Institute of Physical Chemistry Blas Cabrera, CSIC, Madrid 28006, Spain
[3] Department of Civil and Environmental Engineering, The Hong Kong Polytechnic University, Hong Kong, China
[4] Lancaster Environment Centre, Lancaster University, Lancaster, UK
[5] Global Monitoring Laboratory, National Oceanic and Atmospheric Administration, Boulder, CO, USA
[6] Department of Chemistry, University of California, Irvine, CA, USA
[7] Department of Meteorology and Atmospheric Science, Pennsylvania State University, University Park, PA, USA
[8] Research Aviation Facility, Earth Observing Laboratory, NSF National Center for Atmospheric Research, Boulder, CO, USA

Corresponding author: Behrooz Roozitalab (behroozr@ucar.edu), Eric C. Apel (apel@ucar.edu)

Key Points:

- Coincident global scale airborne data from multiple instruments of chlorinated very short-lived substances (Cl-VSLS) provide insights into their distributions and inter-comparability of measurements.

- The updated model reasonably simulates the global distribution of the major Cl-VSLS species and their relative contributions to the tropospheric chlorine burden.

- Model results show a disproportionately high impact of Asian Cl-VSLS emissions regionally and globally throughout the troposphere.

32   **Abstract**

33   Chlorinated very short-lived substances (Cl-VSLS) are ubiquitous in the troposphere and can

34   contribute to the stratospheric chlorine budget. In this study, we present measurements of

35   atmospheric dichloromethane (CH_2Cl_2), tetrachloroethene (C_2Cl_4), chloroform ($CHCl_3$), and 1,2-

36   dichloroethane (1,2-DCA) obtained during the National Aeronautics and Space Administration

37   (NASA) Atmospheric Tomography (ATom) global-scale aircraft mission (2016-2018), and use

38   the Community Earth System Model (CESM) updated with recent chlorine chemistry to further

39   investigate their global tropospheric distribution. The measured global average Cl-VSLS mixing

40   ratios, from 0.2 to 13 km altitude, were 46.6 ppt (CH_2Cl_2), 9.6 ppt ($CHCl_3$), 7.8 ppt (1,2-DCA),

41   and 0.84 ppt (C_2Cl_4) measured by the NSF NCAR Trace Organic Analyzer (TOGA) during

42   ATom. Both measurements and model show distinct hemispheric gradients with the mean

43   measured Northern to Southern Hemisphere (NH/SH) ratio of 2 or greater for all four Cl-VSLS.

44   In addition, the TOGA profiles over the NH mid-latitudes showed general enhancements in the

45   Pacific basin compared to the Atlantic basin, with up to ~18 ppt difference for CH_2Cl_2 in the mid

46   troposphere. We tagged regional source emissions of CH_2Cl_2 and C_2Cl_4 in the model and found

47   that Asian emissions dominate the global distributions of these species both at the surface (950

48   hPa) and at high altitudes (150 hPa). Overall, our results confirm relatively high mixing ratios of

49   Cl-VSLS in the UTLS region and show that the CESM model does a reasonable job of

50   simulating their global abundance but we also note the uncertainties with Cl-VSLS emissions

51   and active chlorine sources in the model. These findings will be used to validate future emission

52   inventories and to investigate the fast convective transport of Cl-VSLS to the UTLS region and

53   their impact on stratospheric ozone.

54   **Plain Language Summary**

55   The Montreal Protocol has phased down the consumption and production of a large number of

56   halogenated compounds such as CFCs, due to their potential for depleting stratospheric ozone.

57   However, the consumption and production of a class of halogenated compounds, referred to as

58   very short-lived substances (VSLS), is not controlled by the Montreal Protocol. Evidence is

59   growing that globally increasing emissions of human-produced chlorinated VSLS (Cl-VSLS)

60   could have an impact on stratospheric ozone. In this work, we present comprehensive aircraft

61   measurements coupled to modeling of the major speciated Cl-VSLS that show their present day

62 global distribution at altitudes up to 12 km and also show that Asian emissions are responsible

63 for the majority of observed Cl-VSLS throughout the troposphere including the Southern

64 Hemisphere.

1. Introduction

66 Very short-lived substances (VSLS) include the class of halogen (Cl, Br, and I) containing

67 substances that have atmospheric lifetimes typically less than six months. While the majority of

68 VSLS emissions are photochemically destroyed in the troposphere during their lifetime, the

69 *Scientific Assessment of Ozone Depletion* reports – as early as the 1998 edition – have shown that

70 these species do enter the stratosphere and affect the stratospheric ozone layer, with the latest

71 findings reported in the 2022 edition (hereafter called SAOD-2022) by Laube et al. (2022).

72 Unlike brominated VSLS (Br-VSLS) which are primarily emitted by natural sources (Carpenter

73 and Liss, 2000; Keng et al., 2021), chlorinated VSLS (Cl-VSLS) have significant anthropogenic

74 sources (Keene et al., 1999; Claxton et al., 2020) and their relative importance is increasing as

75 their estimated contribution to the total stratospheric chlorine abundance has increased from ~2%

76 in 2000 to ~3.4% in 2017 (Hossaini et al., 2019). This increase is attributed to both reduction of

77 long-lived chlorocarbons and growth of Cl-VSLS abundance (Hossaini et al., 2019).

78 Specifically, the sum of total chlorine from VSLS in the stratosphere (through source gas

79 injection + product gas injection) has increased from 80 parts per trillion (ppt) in 1993 to 130 ppt

80 in 2020 (Laube et al., 2022). In addition, although chlorine is reported to be 45-74 times less

81 efficient than bromine in destroying ozone based on several modeling studies (Daniel et al.,

82 1999; Sinnhuber et al., 2009; Klobas et al., 2020), Cl-VSLS could be as important as Br-VSLS

83 due to their high mixing ratios. For example, Oram et al. (2017) observed high Cl-VSLS mixing

84 ratios at the surface over eastern Asia (median of 755.8 ppt of chlorine in Taiwan) which are

85 about 116 times higher than reported Br-VSLS in the SAOD-2022 (Laube et al., 2022). Oram et

86 al. (2017) also reported high concentrations of Cl-VSLS in tropical regions over the western

87 Pacific Ocean, where they can be rapidly uplifted to the upper troposphere. Additionally, it is

88 shown that keeping the Cl-VSLS flux constant (compared to a zero Cl-VSLS flux scenario) will

89 delay the return date of total column ozone to 1980 levels by approximately seven years

90 (Dhomse et al., 2019; Chipperfield et al., 2020; Laube et al., 2022). Long-lived chlorinated

91 ozone depleting substances (ODSs; i.e., CFCs, HCFCs, etc.) have been overall successfully

92   controlled under the Montreal Protocol. Hence, a better understanding of the sources, global

93   abundance, distribution, and transport of Cl-VSLS to the stratosphere has become more crucial

94   to ensure that their trends do not slow down the progress made in reducing atmospheric Cl and

95   Br abundance and significant progress has been made in addressing this issue (Pan et al., 2017;

96   Feng et al., 2018; Hossaini et al., 2019; Claxton et al., 2020; Adcock et al., 2021; An et al., 2021;

97   Keng et al., 2021; Lauther et al., 2022; Thompson et al., 2022).

98   The most abundant Cl-VSLS in the atmosphere are dichloromethane (CH_2Cl_2), chloroform

99   ($CHCl_3$), 1,2-dichloroethane (CH_2ClCH_2Cl, herein referred to as 1,2-DCA) and tetrachloroethene

100   (C_2Cl_4). The atmospheric lifetimes of these Cl-VSLS differ regionally with the longest lifetimes

101   at high latitudes and altitudes. The SAOD-2022 reported both an average (and a range) for their

102   lifetimes: 1,2-DCA = 81.3 days (41–555 days) and C_2Cl_4 = 109 days (66–245 days), $CHCl_3$ =

103   178 days (97–1145 days), and CH_2Cl_2 = 176 days (95–1070 days). $CHCl_3$, has significant

104   emissions by natural sources (Worton et al., 2006; Feng et al., 2018), but the other three

105   atmospherically abundant Cl-VSLS compounds are largely (about 90%) anthropogenic (Laube et

106   al., 2022) and primarily used in industry. $CHCl_3$ also has industrial sources and is used in

107   chemical manufacturing; its global emission trend between 2010 and 2015 is explained entirely

108   by increasing emissions in eastern Asia (Fang et al., 2019). Nevertheless, long-term ground

109   observations by the Advanced Global Atmospheric Gases Experiment (AGAGE) network

110   suggest $CHCl_3$ is currently stable; its annual mean mole fraction remained constant at 8.7 ppt in

111   2019 and 2020 (Laube et al., 2022).

112   CH_2Cl_2 is a co-product of industrial production of $CHCl_3$ and is used as a versatile chemical

113   solvent and degreasing agent (Feng et al., 2018). It had global annual mean mole fractions of

114   38.3 and 45.5 ppt in 2020 based on the AGAGE and National Oceanic and Atmospheric

115   Administration (NOAA) networks, respectively (Laube et al., 2022). Asia is currently recognized

116   to be the main source region of CH_2Cl_2 with the largest contributions from China and India

117   (Feng et al., 2018; Say et al., 2019; An et al., 2021). It has been estimated that Asian emissions

118   of CH_2Cl_2 increased annually by 51 Gg yr^{-1} from 2006 to 2017 (Claxton et al., 2020). Sustained

119   growth in the atmospheric CH_2Cl_2 mole fraction in coming decades could delay the recovery of

120   stratospheric ozone over Antarctica (Hossaini et al., 2017). However, the rate of increase of

121   global abundance of CH_2Cl_2 slowed after 2016, potentially due to regulatory control and

122   economic drivers (An et al., 2021; Laube et al., 2022).

123   C_2Cl_4, with annual global mole fractions in the low ppt range, is used as both a dry cleaning

124   solvent and industrial precursor (Simpson et al., 2004; Laube et al., 2022). Unlike CH_2Cl_2,

125   emissions of C_2Cl_4 are of the same order in Asia, North America, and Europe (Claxton et al.,

126   2020). While C_2Cl_4, with four Cl atoms, has the largest number of Cl atoms per molecule

127   amongst the Cl-VSLS discussed, it has a shorter lifetime than CH_2Cl_2 and the emissions of this

128   toxic compound have declined in recent years owing to controls in different countries on its use

129   (Claxton et al., 2020). Similarly, 1,2-DCA which is most commonly used in the production of

130   vinyl chloride (chloroethene), is also a toxic compound. Although not much is known about its

131   global budget as it is not reported by long-term observations networks, limited observations

132   suggest it is the second most abundant Cl-VSLS after CH_2Cl_2 and in some regions of the

133   atmosphere it has a very large abundance (Oram et al., 2017; Laube et al., 2022). Oram et al.

134   (2017) reported 1,2-DCA ground-level mole fractions up to 309 ppt in Taiwan and estimated its

135   annual Asian emissions at about 203 Gg, based on CH_2Cl_2 emissions and its positive correlation

136   with 1,2-DCA measurements.

137   Due to their non-uniform emissions and relatively short lifetimes, Cl-VSLS have large variability

138   in their global tropospheric distribution (zonally, meridionally, and vertically), with higher mole

139   fractions close to their source regions. CH_2Cl_2 ground measurements show up to 3.5 times higher

140   mole fractions in the Northern Hemisphere (NH) than in the Southern Hemisphere (SH) (Laube

141   et al., 2022). Additionally, a large vertical gradient is reported over the tropics with sharper

142   slopes for shorter-lived VSLS species (e.g. C_2Cl_4) (Andrews et al., 2016; Pan et al., 2017). Also,

143   there is a significant difference between the global CH_2Cl_2 mean mole fractions reported by

144   AGAGE and NOAA networks, only some of which could be explained by calibration

145   differences, suggesting an impact due to differing sampling locations (Laube et al., 2022). Since

146   the measurements by global networks are also used for developing top-down emission estimates,

147   the limited spatial coverage of measurement stations leads to differences between top-down and

148   bottom-up inventories (An et al., 2021). Similarly, most airborne campaigns that measured VSLS

149   within the last decade focused on specific regions or times of the year (Leedham Elvidge et al.,

150   2015; Oelhaf et al., 2019; Keber et al., 2020; Adcock et al., 2021; Jesswein et al., 2022). In

151   particular, the CAST (Coordinated Airborne Studies in the Tropics), CONTRAST (CONvective

152   TRansport of Active Species in the Tropics), and ATTREX (Airborne Tropical TRopopause

153   EXperiment) airborne studies measured Cl-VSLS over the tropical western Pacific Ocean during

154   January and February 2014 (Andrews et al., 2016; Harris et al., 2017; Pan et al., 2017).

155   Additionally, the ORCAS (O_2/N_2 Ratio and CO_2 Airborne Southern Ocean Study) airborne study

156   (January–February 2016) measured Cl-VSLS over the Southern Ocean (Stephens et al., 2018). In

157   contrast, this study is focused on measurements made during the NASA Atmospheric

158   Tomography (ATom) mission (Thompson et al., 2022), a recent global-scale multi-year mission

159   (2016–2018), which included observations of Cl-VSLS from the NCAR Trace Organic Gas

160   Analyzer (TOGA), the University of California, Irvine Whole Air Sampler (UCI WAS), and the

161   NOAA Programmable Flask Package (PFP) instruments, throughout all four seasons, to

162   characterize their global chemistry and transport.

163   Halogens have a broad range of impacts on atmospheric chemistry, including catalytic loss of

164   tropospheric ozone. In particular, rapid cycling between halogen radicals and their reservoirs

165   converts NO_x to HNO_3, reducing ozone concentrations, which further affects the OH abundance

166   as the principal atmospheric oxidant (Simpson et al., 2015; Wang et al., 2021; Li et al., 2022).

167   The recent addition of halogen chemistry to global models has enabled scientists to better

168   understand the global impact of chlorine sources on atmospheric chemistry (Ordóñez et al.,

169   2012; Saiz-Lopez and von Glasow, 2012; Fernandez et al., 2014; Simpson et al., 2015; Wang et

170   al., 2021). Hossaini et al. (2016) updated the tropospheric chlorine chemistry in the TOMCAT

171   model, which was used later by Claxton et al. (2020) to constrain the global emissions of CH_2Cl_2

172   and C_2Cl_4 based on available atmospheric long-term and campaign-based measurements.

173   Hossaini et al. (2019), Chipperfield et al. (2018), and Chipperfield et al. (2020) used this updated

174   TOMCAT model to investigate the trend of stratospheric chlorine from Cl-VSLS, their impact

175   on lower stratospheric ozone, and ozone layer recovery, respectively. Li et al. (2022) updated the

176   halogen chemistry in the Community Earth System Model (CESM) and studied the impact of

177   halogens on the global methane burden. Nevertheless, prior to this study a comprehensive

178   evaluation of the global models in reproducing the global distribution and seasonal variation of

179   Cl-VSLS had not been performed.

180   In this work, we present the spatial and vertical distribution of CH_2Cl_2, C_2Cl_4, 1,2-DCA, and

181    $CHCl_3$ measured by the TOGA, WAS, and PFP instruments during ATom. We highlight the

182   latitudinal and seasonal variability of Cl-VSLS and use tracers to understand their distributions

183   and interhemispheric difference. The CESM model with updated chlorine chemistry is used to

184   simulate the Cl-VSLS during the ATom mission period and the model output is compared with

185 the measurements. We also evaluate the model results against co-located AGAGE and NOAA

186 ground-site observations and use the reaction rate information from the model output to

187 investigate the dominant photochemical destruction pathways of Cl-VSLS. Finally, we tag the

188 emissions in different regions of the world to estimate their impact on global tropospheric

189 abundance of Cl-VSLS.

190
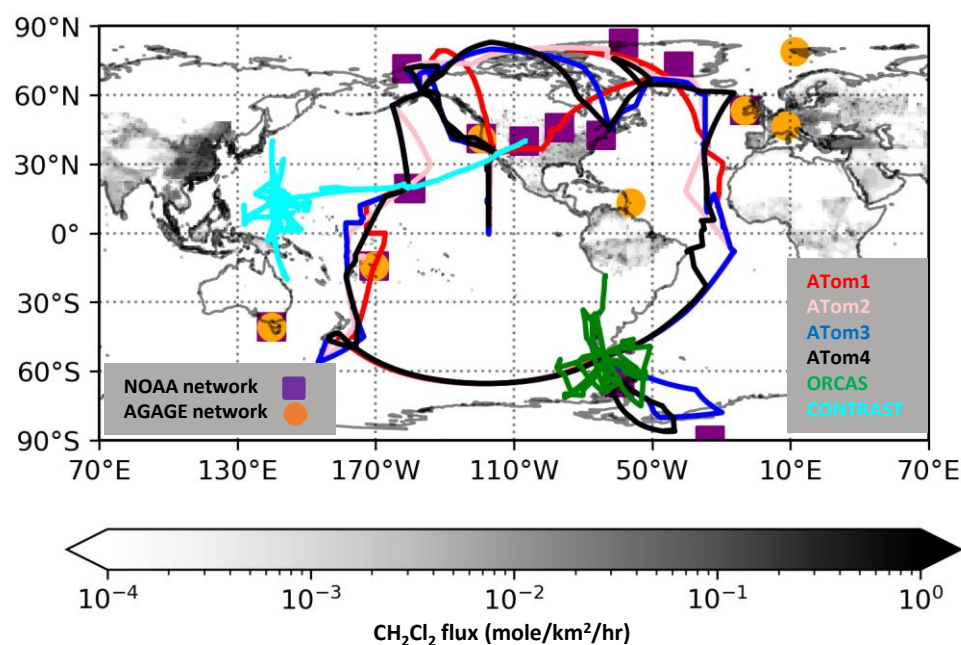
Figure 1. Map of the flight tracks for individual ATom deployments, and ORCAS and CONTRAST missions. The
ground measurement sites in the NOAA and AGAGE networks used in this study are also shown. The map is
shaded by the 2016 annual average CH_2Cl_2 emissions developed by Claxton et al. (2020).

2. Methods

2.1. Measurements

This work is primarily based on observations made during the NASA ATom mission. ATom was

a global-scale mission that flew the heavily instrumented NASA DC-8 aircraft over remote

regions during four seasons between 2016 and 2018 (Thompson et al., 2022). Specifically,

ATom collected measurements, with regular profiling between 200 m and ~13 km altitude, from

28 July to 22 August 2016 (ATom-1), 26 January to 22 February 2017 (ATom-2), 28 September

to 26 October 2017 (ATom-3), and 24 April to 21 May 2018 (ATom-4). In this work, we assign

each ATom deployment to the month with the majority of data, e.g., August 2016 for ATom-1.

This mission provides a comprehensive dataset to characterize the chemistry and transport of

204   chemical species in the remote regions of the troposphere and the UTLS (upper troposphere and

205   lower stratosphere). We specifically present the Cl-VSLS data measured during the ATom

206   mission. In addition, we compare ATom data with our TOGA measurements made during

207   ORCAS and CONTRAST and use surface observation data measured by ground monitoring

208   networks around the globe to complement the evaluation of the model performance.

209   Table 1 summarizes the measurements used in this study.

210   **2.1.1.   ATom Cl-VSLS observations**

211   As shown in Figure 1, the ATom mission consisted of four deployments with very similar near-

212   pole-to-pole flight tracks over remote regions with regular profiling throughout much of the

213   troposphere, which provides a unique dataset to better understand the spatial and seasonal

214   variations of Cl-VSLS. Within these deployments, three systems provided measurements of Cl-

215   VSLS mixing ratios: 1) the NCAR Trace Organic Gas Analyzer (TOGA) instrument, 2) the

216   University of California, Irvine Whole Air Sampler (UCI WAS), and 3) the NOAA

217   Programmable Flask Package (PFP).

218   The three systems used in this study to measure Cl-VSLS, have been previously documented in

219   the literature and will only be briefly described here. TOGA is an *in-situ* fast gas chromatograph

220   quadrupole mass spectrometer (GC/MS) that continuously measures a wide range of VOCs.

221   During ATom, TOGA analyzed samples collected over 35 seconds every 2 minutes (Apel et al.,

222   2015). The UCI WAS (Simpson et al., 2010) had 168 electropolished stainless steel (SS)

223   canisters on board for each flight and collected pressurized whole air samples throughout the

224   flights, sampling every 2–5 minutes for between 20 seconds to 2 minutes in duration, pressure

225   altitude dependent. Post flight, the canisters were returned to the UCI laboratory where they were

226   analysed using a series of gas chromatographs. Likewise, the NOAA PFP (Hu et al., 2015;

227   Sweeney et al., 2015) system collected whole air samples in up to 24 glass flasks per flight (48

228   flasks during ATom-2), typically averaging one 10-s to 20-s sample every 10–20 minutes. These

229   flasks were returned to the NOAA laboratory for analysis by gas chromatography with mass

230   spectrometric detection. Data obtained from all three methodologies were used to analyze results

231   for a large suite of VOCs, including Cl-VSLS. TOGA uses NOAA calibration scales and on-

232   board standards and cross calibrates with a multi-component calibration standard from the

233   National Institute of Standards and Technology (NIST). Specifically, TOGA referenced their

234   measurements for CH_2Cl_2 and $CHCl_3$ to the NOAA ESX-3583 standard and referenced their

235   measurements for C_2Cl_4 and 1,2-DCA to the NIST CAL 014921 calibration mixture,

236   respectively. In addition, TOGA used NCAR prepared standards as in-flight working standards

237   for all species. NOAA PFP used their calibration scales for all the compounds including a

238   recently developed NOAA-2019 scale for 1,2-DCA. UCI-WAS data are reported based on their

239   own set of calibration standards and thus their calibration is independent of both NOAA PFP and

240   NCAR TOGA.

241   The TOGA instrument measured 12,168 samples during the four ATom deployments, and WAS

242   and PFP collected and analyzed 6,991 and 1,109 flask samples, respectively. For statistical

243   analyses of the data, we replaced observations below the lower limit of detection (LLOD) with

244     $0.5 \times$ LLOD based on the U.S. EPA guidance for data quality assessment (USEPA, 2000);

245   approximately 15% of TOGA samples were below the LLOD for C_2Cl_4 (Table S1). For

246   comparisons to the observations, the model output was sampled instantaneously along the ATom

247   flight tracks using TOGA sampling times and locations. We use normalized mean bias (NMB),

248   root mean squared error (RMSE), and Pearson correlation coefficient (r) as statistical metrics for

249   evaluation.

250   **2.1.2.**   **Ground-based observations**

251   We used the monthly mean mole fractions of ground-based CH_2Cl_2 and C_2Cl_4 measurements for

252   a three-year period, 2016–2018, from the National Oceanic and Atmospheric Administration

253   (NOAA) and Advanced Global Atmospheric Gases Experiment (AGAGE) monitoring networks

254   (Prinn et al., 2018; Claxton et al., 2020). Specifically, we used data from 14 NOAA and 7

255   AGAGE sites measured using GC/MS systems (the stations used are listed in Table S2). As

256   shown in Figure 1, the majority of these sites are located in the NH, and co-located

257   measurements are made by these networks at four sites (two in each hemisphere). For CH_2Cl_2,

258   the NOAA and AGAGE networks use NOAA-2003 and AGAGE SIO-14 calibration scales; we

259   increased the AGAGE measurements by 10.38% following the known calibration offset between

260   results for this chemical in these networks (Claxton et al., 2020). It is worth mentioning that

261   AGAGE network uses *in-situ* measurement systems, while the NOAA network uses flasks,

262   which are transported and analyzed at the NOAA Global Monitoring Laboratory in Boulder,

263   Colorado.

264   **2.1.3.   Auxiliary data from ORCAS and CONTRAST**

265   We complemented our analysis with Cl-VSLS observations from two additional field campaigns

266   (Figure 1). We used CH_2Cl_2, $CHCl_3$, and C_2Cl_4 data measured by TOGA from the O_2/N_2 Ratio

267   and CO_2 Airborne Southern Ocean Study (ORCAS) and the CONvective TRansport of Active

268   Species in the Tropics (CONTRAST) missions, both deployed on the NSF/NCAR Gulfstream V

269   (GV) aircraft. ORCAS was a six-week study in 2016 (January–February) focused on the

270   Southern Ocean (35–75°S) and collected data by frequently profiling the atmosphere up to ~13

271   km altitude (Stephens et al., 2018). Similarly, during CONTRAST the GV profiled up to ~15 km

272   altitude during a seven-week study in 2014 (January–February), focusing on deep convection in

273   the tropical western Pacific (20°S–40°N) (Pan et al., 2017).

274   **Table** 1. Summary of airborne missions and measurement instruments used in this study.

Instrument	Mission (# of samples)	Methodology	Measurement Details	Inlet Setup	Reported Uncertainties[a]				Ref.
					CH_2Cl_2	C_2Cl_4	$CHCl_3$	1,2-DCA	
NCAR TOGA	ATom (12,168), ORCAS (2573), CONTRAST (3568)	*in situ* Fast GC/MS	35-s samples every 2 min	Heated Sulfinert® tubing	± 15%	± 30%	± 15%	± 30%	Apel et al. (2015)
UCI WAS	ATom (6,991)	Stainless steel flask collection and laboratory analysis by multi-detector GC	Variable – flasks sampled on demand (average 45-s sample every 3.5 min)	Unheated stainless steel	± 20%	± 20%	± 20%	± 25%	Simpson et al. (2010)
NOAA PFP	ATom (1,121)	Glass flask collection and laboratory analysis by GC/MS	Variable – flasks sampled on demand (average 15-s sample every 10-20 min)	Chemically-passivated SS tubing	± 10%	± 15%	± 20%	± 15%	Sweeney et al. (2015); Hu et al. (2015)

275   [a] The uncertainties reported here represent the combination of estimated scale uncertainties and measurement
276   precision.

277   **2.2. Simulations**

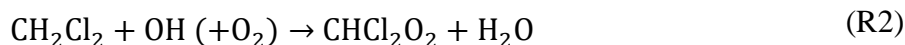278   **2.2.1.   Model configuration**

279   CESM is a coupled climate/Earth system modeling framework with different components

280   including land and atmosphere (Hurrell et al., 2013). CAM-chem, the Community Atmosphere

281   Model with Chemistry, is the atmospheric component of CESM that solves the physics,

282 dynamics, and chemistry of the troposphere and stratosphere (Lamarque et al., 2012). The online

283 interaction between meteorology, thermodynamic processes, and chemistry makes CESM an

284 appropriate model to study the global distribution and transport of VSLS (Wang et al., 2019a).

285 The version of CAM-chem (based on CESM1) used in this study is based on the Community

286 Atmosphere Model, version 4 (Neale et al., 2013; Tilmes et al., 2016), in which the hydroxyl

287 radical (OH) abundance is calculated online (i.e., not prescribed). The horizontal resolution is

288 $0.9° \times 1.25°$ (latitude $\times$ longitude) with 56 vertical levels in a hybrid sigma-pressure system. The

289 top boundary of the model is at 3 hPa ($\approx$ 40 km). We ran the model for three years 2016–2018

290 (after two years of spin-up) in specified dynamics mode, in which the temperature and horizontal

291 winds are nudged with a 50-h relaxation time towards data from NASA's Modern-Era

292 Retrospective analysis for Research and Applications, Version 2 (MERRA-2) (Gelaro et al.,

293 2017). The anthropogenic emissions are from the Copernicus Atmosphere Monitoring Service

294 global emission inventory version 5.1 (CAMSv5.1) and Coupled Model Intercomparison Project

295 Phase 6 (Hoesly et al., 2018; Granier et al., 2019), biomass burning emissions are from the Fire

296 Inventory from NCAR, version 2.5 (FINN v2.5) based on MODIS fire detections (Wiedinmyer

297 et al., 2023), and emissions from vegetation are calculated online in the land component of the

298 model (CLM) based on the Model of Emissions of Gases and Aerosols from Nature (MEGAN;

299 Guenther et al. (2012)). For CH_2Cl_2 and C_2Cl_4 emissions, we used the recently-developed

300 emission inventory by Claxton et al. (2020). They constrained the long-term global emissions of

301 these two species up to 2017 (with no seasonality) based on a combination of long-term

302 observation data, recent bottom-up emissions for Asia, and Reactive Chlorine Emissions

303 Inventory (RCEI) framework for other regions, which led to improved modeling results (we

304 extrapolated the emissions for the year 2018). The RCEI was a pioneering effort to produce the

305 gridded global emission inventory of chlorinated species, which enabled assessment of

306 atmospheric chlorine cycle (Keene et al., 1999). A latitude-dependent lower boundary condition

307 (LBC) for $CHCl_3$ and 1,2-DCA was prescribed with higher values in the NH (Hossaini et al.,
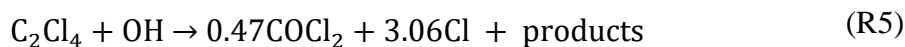
308 2016).

309 The tropospheric and stratospheric chemistry scheme is based on the MOZART-4 chemical

310 mechanism implemented in CAM4-chem (Kinnison et al., 2007; Emmons et al., 2010; Tilmes et

311 al., 2016). In addition, we used an updated VSLS chemistry scheme that includes the four Cl-

312 VSLS, specifically CH_2Cl_2, C_2Cl_4, $CHCl_3$, and 1,2-DCA. This scheme is based on the halogen

313   chemistry mechanism implemented by Ordóñez et al. (2012) and includes updates on halogen

314   heterogeneous reactions and rate constants (Fernandez et al., 2014; Saiz-Lopez et al., 2014; Li et

315   al., 2022). These updates will be included in the upcoming CESM2.3 release. The photochemical

316   destruction pathways for the four Cl-VSLS are through reactions with OH and chlorine atom (Cl)

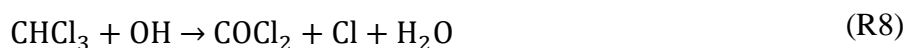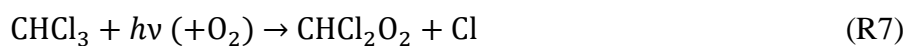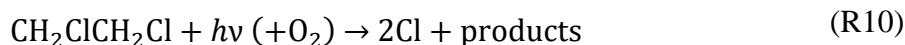317   and photolysis ($h\nu$) as shown below (R1–R12) (Hossaini et al., 2016).

CH_2Cl_2:

$$CH_2Cl_2 + h\nu \rightarrow 2Cl \ + \ products \tag{R1}$$

$$CH_2Cl_2 + OH \ (+O_2) \rightarrow CHCl_2O_2 + H_2O \tag{R2}$$

$$CH_2Cl_2 + Cl \ (+O_2) \rightarrow CHCl_2O_2 + HCl \tag{R3}$$

C_2Cl_4:

$$C_2Cl_4 + h\nu \rightarrow 4Cl + \ products \tag{R4}$$

$$C_2Cl_4 + OH \rightarrow 0.47COCl_2 + 3.06Cl \ + \ products \tag{R5}$$

$$C_2Cl_4 + Cl + M \rightarrow 5Cl \ + \ products \tag{R6}$$

$CHCl_3$:

$$CHCl_3 + h\nu \ (+O_2) \rightarrow CHCl_2O_2 + Cl \tag{R7}$$

$$CHCl_3 + OH \rightarrow COCl_2 + Cl + H_2O \tag{R8}$$

$$CHCl_3 + Cl \rightarrow COCl_2 + Cl + HCl \tag{R9}$$

1,2-DCA:

$$CH_2ClCH_2Cl + h\nu \ (+O_2) \rightarrow 2Cl + products \tag{R10}$$

$$CH_2ClCH_2Cl + OH \ \rightarrow 2Cl + H_2O \tag{R11}$$

$$CH_2ClCH_2Cl + Cl \rightarrow 2Cl + HCl \tag{R12}$$
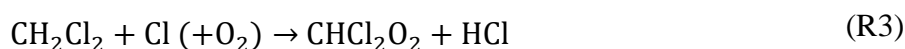
318   **2.2.2.**   **Tagged species**

319   Tagged tracers are artificial emitted species treated as the replica of original tracers, going

320   through similar reactions in the chemical mechanism and continuity equations as the original

321   tracers, while not affecting the interactive chemistry of the atmosphere (Emmons et al., 2012).

322   To study different source regions' contributions to the atmospheric abundance of anthropogenic

323   Cl-VSLS, we tagged CH_2Cl_2 and C_2Cl_4 emissions in the model simulation. Note that $CHCl_3$ and

324   1,2-DCA were based on LBC in this work and hence not tagged. We tagged CH_2Cl_2 and C_2Cl_4

325   emitted from Asia (AS), Europe (EU), North America (NA), South America (SA), and Africa

326   (AF). Additionally, we assigned emissions outside these regions as the rest of the world (ROW)

327   tracers. As a result, we implemented a total of 12 tagged tracers in the model. The emission

328   magnitudes from each region of the tagged tracer was equal to the emission of that specific

329   region in the original tracer emission inventory. Figure S1 shows that AS emissions are the

330   dominant emission source of CH_2Cl_2 while AS, EU, and NA emissions of C_2Cl_4 are of the same

331   order of magnitude. These tagged emissions go through photolysis, reaction with OH, and

332   reaction with Cl. The primary source of inorganic chlorine in the model is through the

333   heterogeneous reactions of halogenated species and sea salt aerosol (SSA) as well as

334   mobilization of Cl^- from SSA through acid displacement (following Li et al., 2022). We use

335   these emissions to estimate the tropospheric Cl-VSLS budgets due to different sources.

3. Results and discussion

3.1. Vertical and spatial distribution of Cl-VSLS

The vertical profiles of measured CH_2Cl_2, C_2Cl_4, $CHCl_3$, and 1,2-DCA mixing ratios in different latitude bins for all the samples analyzed during ATom-1 through ATom-4 are shown in
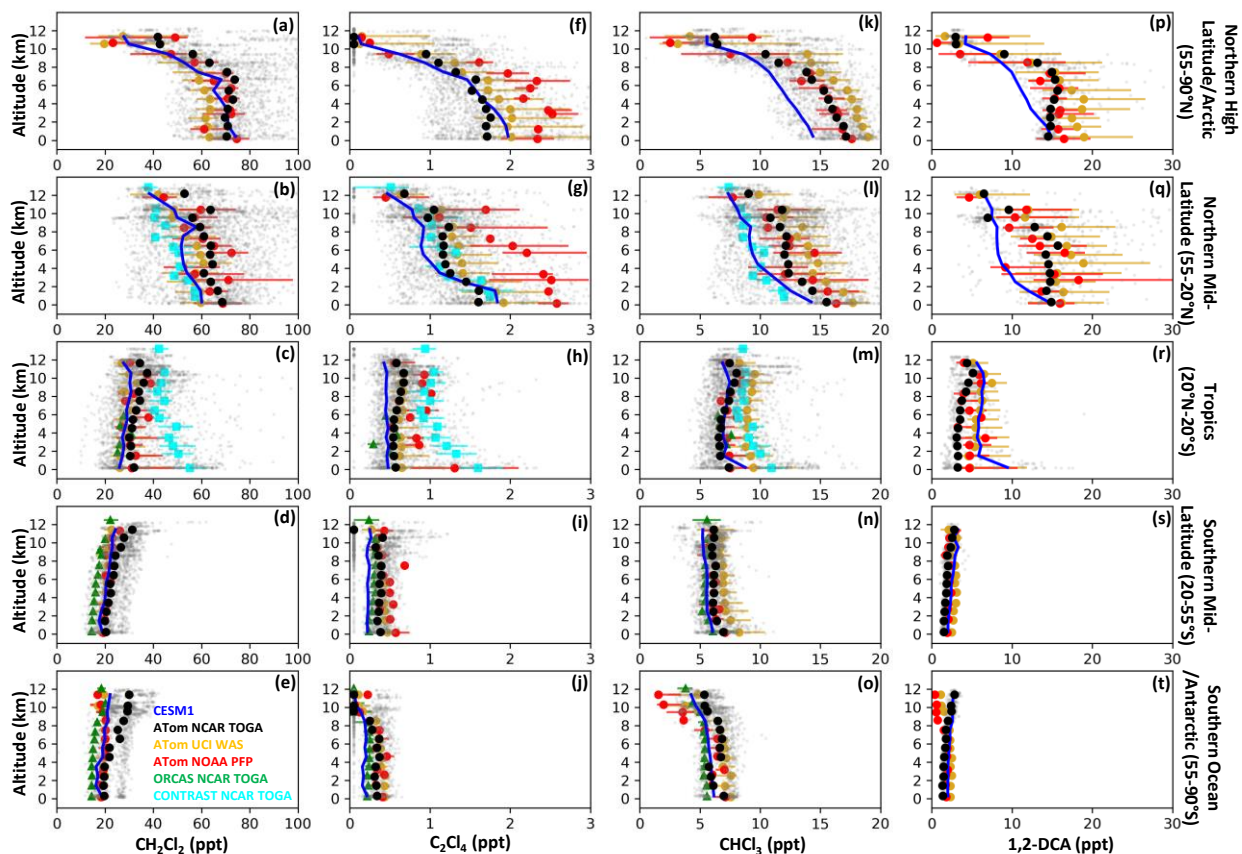
Figure 2 (vertical profiles for individual ATom deployments are shown in the supporting information; Figures S2–S5). In this section, we focus only on the measured data and different instruments, and the model performance is discussed in Section 3.3. The general trend for all the species is that the mixing ratios in the NH are higher than the SH. For example, the average ($\pm$ standard deviation) of the measured CH_2Cl_2 mixing ratios by TOGA, within the vertical profile and all latitudes of the NH and SH (including their subtropical regions), were 59 ± 22 and 26 ± 7 ppt, respectively. Hossaini et al. (2017) found the NH to SH ratio (NH/SH) of 3 in mid-latitudes for CH_2Cl_2, based on data from ground measurement networks, which is within the *in-situ* NH/SH possible range of our TOGA measurements (1.1–4.3).

350   Similarly, for C_2Cl_4, the mean mixing ratios in the NH and SH were 1.1 ± 0.6 and 0.3 ± 0.2 ppt,

351   respectively. These C_2Cl_4 mixing ratios are significantly lower than those reported in the 20th

352   century (Simmonds et al., 2006), consistent with its declining emission trend (Claxton et al.,

353   2020). For example, Wiedmann et al. (1994) reported mean NH and SH C_2Cl_4 values of 21 ± 5

354   ppt and 2.2 ± 0.5, respectively, for the period between 1982 and 1989. TOGA data for 1,2-DCA

355   (during ATom-4) shows mixing ratios of 12 ± 7 and 2 ± 1 in NH and SH, respectively,

356   supporting the idea of their predominant NH sources, which are believed to be dominated by

357   anthropogenic sources (Oram et al., 2017; Laube et al., 2022).

358   The interhemispheric gradient is also apparent for $CHCl_3$ with an NH/SH ratio of ~2 (1–3.1)

359   during ATom for TOGA data. While anthropogenic sources (i.e., solvents in the industrial

360   sector) are the main source of CH_2Cl_2, 1,2-DCA, and C_2Cl_4 emissions, these sources have

361   historically accounted for less than 30% of emitted $CHCl_3$ (Worton et al., 2006) although a larger

362   anthropogenic contribution is more recently reported (Fang et al., 2019). An increase in NH

363   anthropogenic emissions of $CHCl_3$ between 2011 and 2017 (and a decrease after 2018) was also

364   reported in SAOD-2022 (Laube et al., 2022).

365   There are also regional differences for the Cl-VSLS, primarily over the NH mid-latitudes. Figure

366   3 shows the altitude dependence of Cl-VSLS differences measured over the Pacific and Atlantic

367   Oceans (Pacific minus Atlantic), in 1-km altitude bins. Our measurements show that the NH

368   mixing ratios over the Pacific Ocean are in general higher than those over the Atlantic Ocean.

369   This enhancement is strongest for CH_2Cl_2 with a difference of up to 18 ppt in the mid-

370   troposphere. In addition, the results show a seasonal difference. For example, the results for

371   ATom-2 (May 2017) and ATom-3 (October 2017) are the extremes of the measured differences,

372   in particular for C_2Cl_4 and $CHCl_3$, meaning the smallest and largest differences occurred during

373   these two deployments (see Figure 3b-c).

374   ### 3.1.1. CH_2Cl_2

375   For CH_2Cl_2 in the northern high-latitude region (55–90°N), measurements indicate that the

376   atmosphere is well mixed in the troposphere and there is a strong vertical gradient in the UTLS

377   region. In the northern mid-latitudes (20–55°N), the measured data show a smooth vertical

378   gradient, where the median TOGA measurements decreased, overall, by 1.3 ppt km^{-1} with

379   increasing altitude in contrast with 2.5 ppt km^{-1} in the high latitudes (the mean slope is calculated

380   based on lowest and highest altitude bins). It should be noted that the slopes differ for each

381 ATom deployment (Figure S2). The model captured the seasonal pattern for each ATom

382 deployment (note that emissions do not have seasonality (Claxton et al., 2020)), suggesting that

383 OH abundances control the seasonal trend (i.e., R2 is the main photochemical destruction

384 pathway for CH_2Cl_2 as will be discussed in Section 3.5). Similarly, Claxton et al. (2020) found

385 that their constant monthly emissions were able to generate CH_2Cl_2 seasonality. In the tropics,

386 the CH_2Cl_2 levels are about half of the values for the NH mid- and high latitudes. In addition, the

387 observed tropical mixing ratios are higher at upper altitudes such that the maximum median

388 CH_2Cl_2 value in the profile was at ~10 km. The relatively high mixing ratios in the upper

389 troposphere and reversal of the vertical gradient in the tropics suggest influential impacts of

390 atmospheric dynamics (i.e., transport and convection), pointing to the interhemispheric transport

391 from NH to SH. Similarly in the southern mid-latitudes (20–55°S) and over the Southern Ocean

392 (55–90°S) TOGA CH_2Cl_2 mixing ratios were higher in the upper troposphere than the lower

393 troposphere (inversion with slope ~ -0.9 ppt km^{-1}, where a negative slope indicates increasing

394 levels with increasing height).

395 The CH_2Cl_2 observations from all three instruments (TOGA, WAS, and PFP) compare quite well

396 with each other (Figure 2a-e) and lead to a similar conclusion although there are some minor

397 differences in some regions. For example, in the high-latitude Arctic region (Figure 2a), the

398 vertically-binned median CH_2Cl_2 values from TOGA and PFP are in good agreement with each

399 other yet the WAS data are about 10 ppt lower throughout the profile. The comparisons differ

400 somewhat for each ATom deployment (Figure S2). Specifically, during ATom-2, the medians

401 for all three instruments were about 10 ppt from each other within the marine boundary layer

402 (MBL) and very close in the UTLS region. On the other hand, during ATom-3 the median for

403 WAS and PFP CH_2Cl_2 levels were consistent while TOGA was as much as 15 ppt higher. In

404 addition, TOGA and WAS agreed well during ATom-4 while PFP was on the higher end of the

405 measurements. Some additional inconsistencies were observed between TOGA and the flask

406 measurements from PFP and WAS over the southern high latitudes. TOGA measurements above

407 8 km over the Southern Ocean increased with altitude while WAS and PFP measurements

408 showed a decrease, leading to large biases (for example, the CH_2Cl_2 mixing ratio within the 10-

409 km bin (10–11 km altitude) during ATom-4 was 31.5 ppt and 13.8 ppt measured by TOGA and

410 WAS, respectively). As will be discussed in Section 3.3, the model also showed a modest

411   increase, which is consistent with TOGA data although the TOGA data showed a substantially

412   larger increase.

3.1.2.   C$_2$Cl$_4$

414   C$_2$Cl$_4$ mixing ratios are very low (< 5 ppt) everywhere. Nevertheless, C$_2$Cl$_4$ has vertical and

415   spatial gradients similar to CH$_2$Cl$_2$. At high latitudes, median TOGA measurements show a

416   smooth gradient in the troposphere, and transition to below LLOD with a strong gradient in the

417   UTLS region. Similarly, both WAS and PFP measured very small C$_2$Cl$_4$ levels in the UTLS

418   region. However,
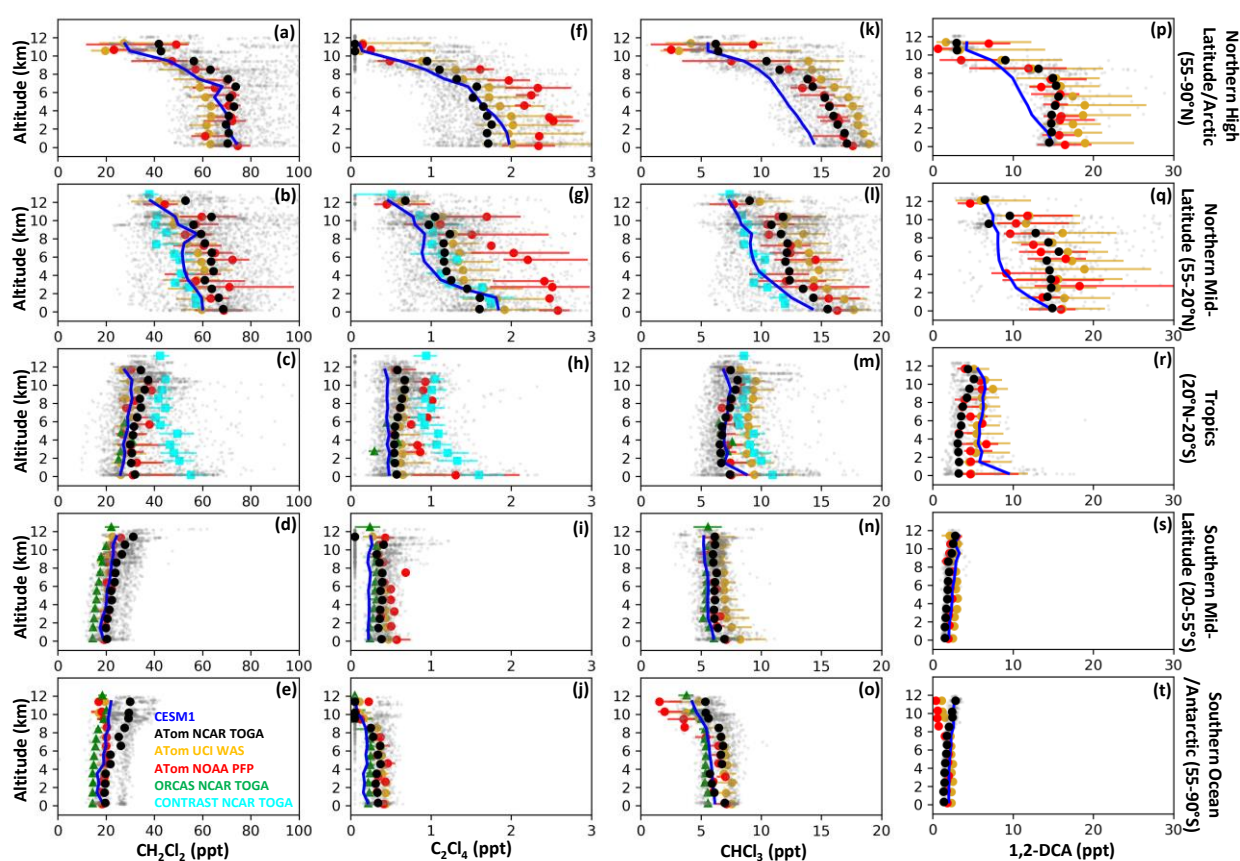
419

420   Figure 2 shows fairly significant differences that are most pronounced in the NH between PFP

421   and the other two instruments that measured C$_2$Cl$_4$, even when only ATom-4 results are

422   considered. This may be due to differences in calibration scales, which we have not pursued

423   further in this work, and may relate to Teflon O-ring contamination of some PFP flask data. It is

424   worth noting that PFP results were reported for C$_2$Cl$_4$ only during the ATom-4 deployment

425   (Figure S3). In northern mid-latitudes, the median TOGA C$_2$Cl$_4$ levels decreased with increasing

426   altitude down to 0.7 ppt above 10 km. In the tropics, median high-altitude C_2Cl_4 mixing ratios

427   were slightly higher than at low altitudes. However, the median data during the ATom mission

428   (for all three measurement systems) did not show an inverted vertical gradient in the SH.

429   Nevertheless, a wider range of mixing ratios (gray dots) was seen at high altitudes in the

430   southern mid-latitudes (
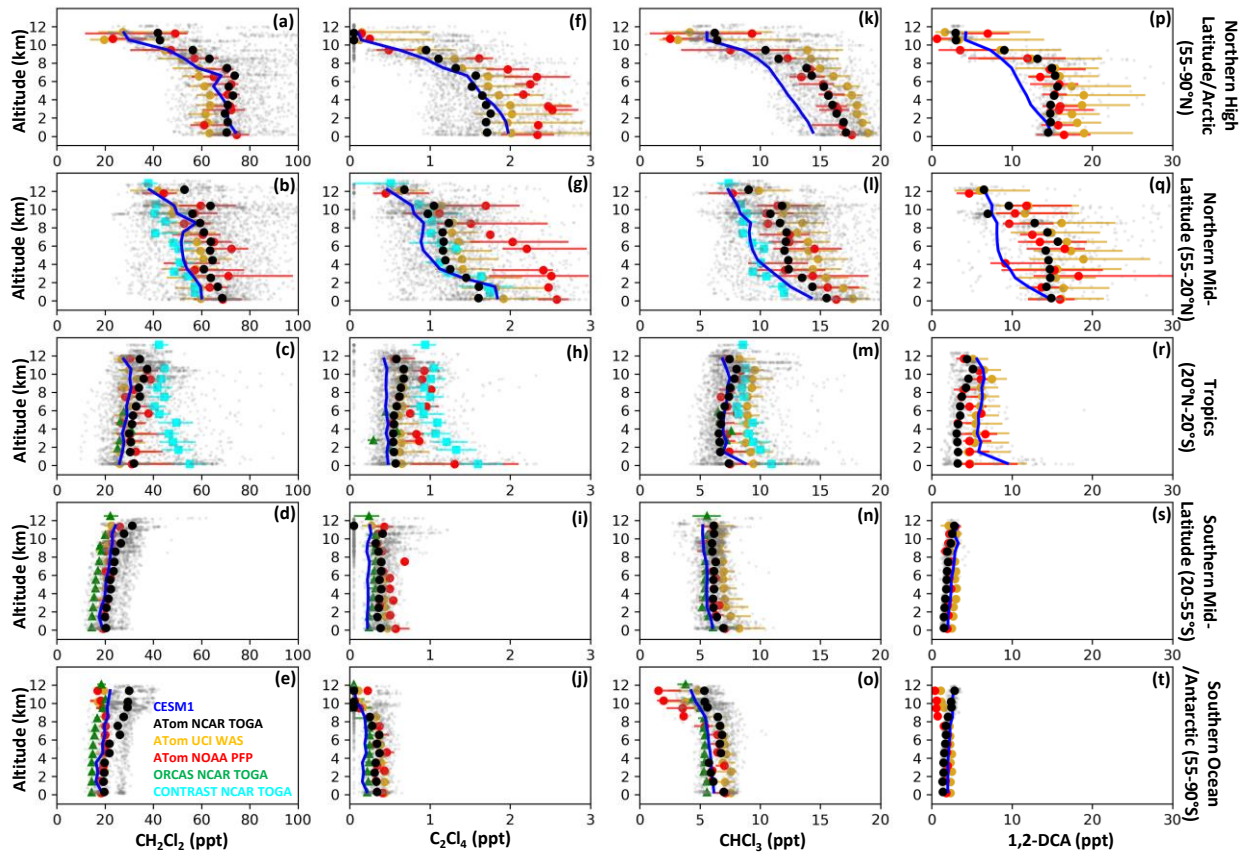
431

432   Figure 2i) with mixing ratios reaching > 1 ppt, suggesting an inversion, with less intensity but

433   similar to CH_2Cl_2 data.

434   **3.1.3.   CHCl₃**

435   The observed CHCl₃ mixing ratios also showed a vertical gradient in the NH (
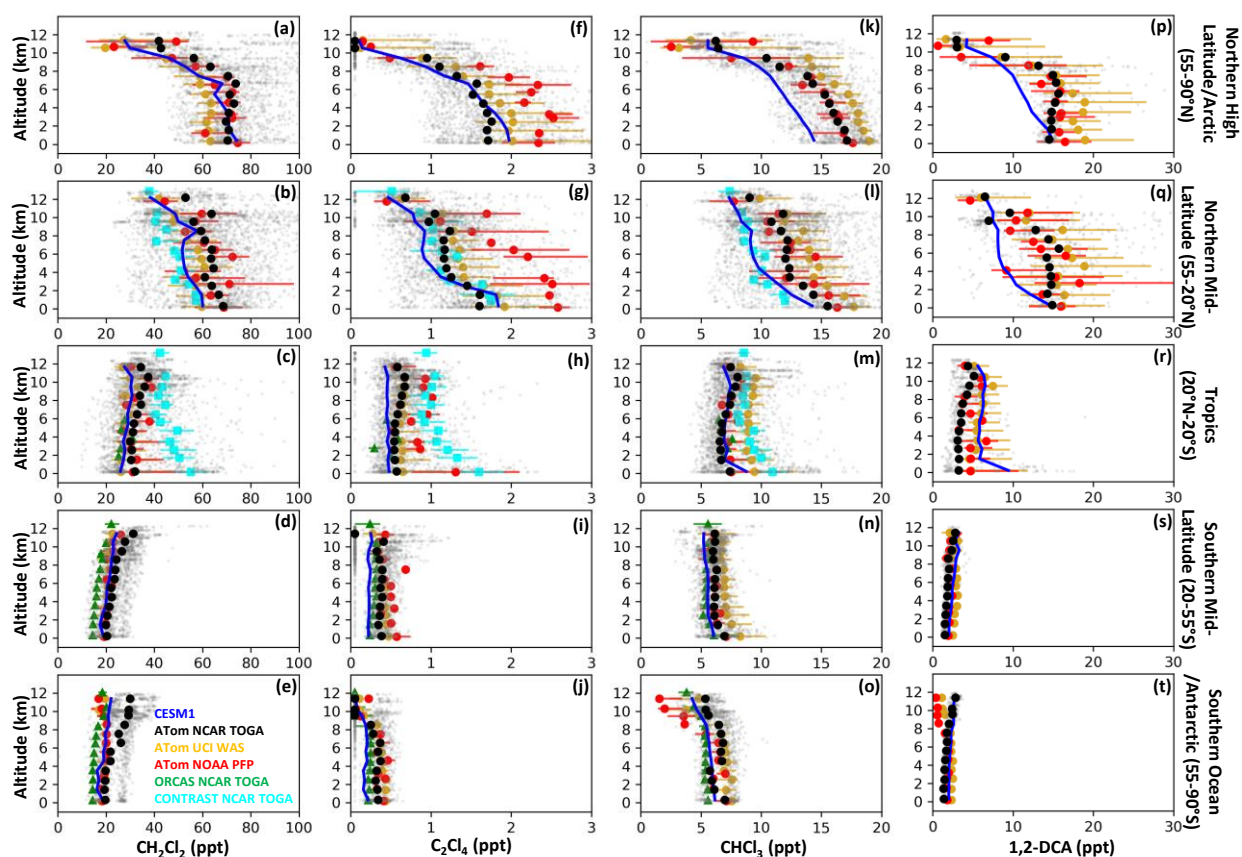
436

437   Figure 2k,l). However, unlike the predominantly anthropogenically-emitted CH_2Cl_2 and C_2Cl_4,

438   the low-altitude $CHCl_3$ levels are modestly higher in the NH high latitudes compared with the

439   mid-latitudes. Specifically, TOGA $CHCl_3$ levels below 3 km in the 60–90°N latitude bin were

440   8% higher than in the 30–60°N latitude bins, with the highest differential measured during

441   ATom-1 (18%). This is in contrast to constant $CHCl_3$ mixing ratios between 30–90°N shown by

442   Prinn et al. (2000), which is used in our model. The global emissions of $CHCl_3$ showed a rapid

443   increase between 2010 and 2017 (Laube et al., 2022), which is attributed to anthropogenic

444   emission increases in China (Fang et al., 2019; An et al., 2023). On the other hand, $CHCl_3$ has

445   major natural sources with higher emissions in the mid-latitude regions (Khalil and Rasmussen,

446   1999). The combined impact of transport of emissions (natural and anthropogenic) and

447   distribution of natural emissions could explain, in part, the higher mixing ratios at 60–90°N. In

448   the tropics, TOGA observed a declining gradient within the MBL, with increasing altitude, and

19

449 an increasing gradient at higher altitudes (i.e., change of the gradient sign), similar to what was

450 observed for CH_2Cl_2 and C_2Cl_4. This inverted "S" shape profile has been also observed for

451 brominated compounds during the CONTRAST mission and was attributed to the convective and

452 advective transport from the surface to the free troposphere (Butler et al., 2018). In the SH, the

453 overall trend suggests a small decreasing gradient although it differs for individual ATom

454 deployments. For example, in the southern mid-latitudes, TOGA measured a decreasing vertical

455 gradient during ATom-1 and ATom-3, and an increasing vertical gradient during ATom-2 and

456 ATom-4. Measurements by WAS and PFP were, in general, consistent with TOGA although

457 WAS reported up to 30% higher mixing ratios during ATom-1 compared with the other two

458 instruments.

459 **3.1.4.   1.2-DCA**

460 The measurements of 1,2-DCA mixing ratios show significant enhancements in the NH (Figure

461 2). In addition, the similar vertical profile shape of 1,2-DCA and CH_2Cl_2 suggests their emission

462 sources are co-located with each other (Oram et al., 2017). Similar to CH_2Cl_2, the Southern

463 Ocean vertical profile of 1,2-DCA between TOGA, WAS, and PFP are different (Figure 2t). The

464 vertical profiles of measured 1,2-DCA for each deployment are in the SI (Figure S5). The

465 SAOD-2018 reported 1,2-DCA as the second most abundant anthropogenic Cl-VSLS, after

466 CH_2Cl_2, in the tropical MBL with a median of 12.8 ppt based on measurements during CAST

467 and CONTRAST in 2013–2014 (Andrews et al., 2016; Pan et al., 2017; Engel et al., 2018).

468 TOGA measurements, Table 2, show that 1,2-DCA mixing ratios during ATom (e.g., 1.8–11.3

469 ppt in the tropical MBL) are lower than that of $CHCl_3$ (e.g., 5.5–12.3 ppt in tropical MBL). Our

470 observations with lower levels of 1,2-DCA compared to $CHCl_3$ may be due to the region studied

471 during CAST and CONTRAST being further west (and closer to the emission sources) and the

472 shorter atmospheric lifetime of 1,2-DCA compared to $CHCl_3$, or due to either decreasing 1,2-

473 DCA emissions or increasing $CHCl_3$ emissions or a difference in measurement calibration.

474 **3.1.5.   Total chlorine during ATom**

475 Overall, there is reasonable agreement between TOGA, PFP, and WAS Cl-VSLS measurements

476 during the ATom mission. In particular, all the measurements agreed within the reported

477 uncertainties. Nevertheless, TOGA provided better data coverage than PFP and WAS as was

478 mentioned in the methods section. As a result, we only use TOGA measurements for the

479   remainder of this paper. The measured TOGA annual global mean mixing ratios ± standard

480   deviations for CH_2Cl_2 (46.6 ± 24.2 ppt), $CHCl_3$ (9.6 ± 4.2 ppt), 1,2-DCA (7.8 ± 7.3 ppt), and

481   C_2Cl_4 (0.84 ± 0.66 ppt) confirm that CH_2Cl_2 is the most abundant Cl-VSLS in the atmosphere.

482   Table 2 summarizes the TOGA-measured anthropogenic Cl-VSLS and total VSLS-sourced

483   chlorine, Cl^{VSLS}, during the ATom mission for different latitude bins and altitude ranges

484   (represented by potential temperature, θ). Here, total Cl^{VSLS} is calculated based on the available

485   chlorine from major Cl-VSLS ($CHCl_3$, CH_2Cl_2, C_2Cl_4, and 1,2-DCA). In the NH and tropics, the

486   highest amount of total Cl^{VSLS} was observed within the MBL (i.e., θ < 320 K). However, the

487   highest values in the SH were found in the upper troposphere (i.e., θ > 340 K), suggesting an

488   interhemispheric transport as discussed below. Within the tropical upper troposphere, the median

489   total Cl^{VSLS} (and range) was 99.6 (76.7–130.5) ppt. Table S3 summarizes the ATom measured

490   mole fractions of ClVSLS, in the tropical upper troposphere, alongside the reported values in the

491   literature (Adcock et al., 2021; Oram et al., 2017; SAOD, 2022). Both the total Cl^{VSLS} and the

492   median mixing ratios of individual Cl-VSLS (i.e., CH_2Cl_2, C_2Cl_4, and $CHCl_3$) in the tropics

493   (Table S3) are close to the range of the reported values in the SAOD-2022 report (Laube et al.,

494   2022). However, the differences for 1,2-DCA were large; ATom data (median of 4.8 ppt) were

495   about 40% lower than SAOD (2022) data (median of 8.3 ppt). On the other hand, the upper

496   bound of measurements in South and East Asia (Oram et al., 2017; Adcock et al., 2021) were

497   significantly high, as they were close to the source regions. For example, the upper bound of

498   CH_2Cl_2 mixing ratios were 136 ppt in South Asia (Adcock et al., 2021), in contrast with 47.5 ppt

499   measured during ATom.

500   **3.1.6.   Uncertainties between instruments**

501   As discussed above, there are some locations with poor agreement between the Cl-VSLS

502   measured by the three instruments, in particular over the Southern Ocean. From our analysis

503   using the five latitude bins shown in Figure 2, the Southern Ocean bin had the lowest average

504   temperatures and water vapor mixing ratios. Above 8 km, the average temperature was 214.8 K

505   and the average water vapor mixing ratio was 25.9 ppm. The latitude bin with next lowest mean

506   water vapor mixing ratio was over the northern high latitudes at 56.2 ppm followed by the

507   southern mid-latitudes at 153.0 ppm.

508   One hypothesis for the instrumental differences is that the measurement biases could be due to

509   losses on either the unheated inlet walls or the canister/flask walls for the WAS and PFP

510   measurements, which can be more pronounced at lower ambient humidities.

511   TOGA uses a heated Sulfinert^{TM} inlet line and does not store the samples prior to analysis. The

512   flask samples (WAS and PFP) are collected by drawing air in through non-heated lines; WAS

513   uses a non-heated stainless steel (SS) line and the PFP uses a coated SS line. For most materials,

514   a threshold level of humidity is needed to keep surfaces properly passivated. Exceptions are in

515   the case of Teflon^{TM} or Silonite^{TM} (Deming et al., 2019) for which there is little absorptive effect

516   even at 0% humidity. Glass and SS also showed to be relatively non-adsorptive although not as

517   good as Teflon^{TM} or Silonite^{TM}. In the Deming et al. (2019) study, Sulfinert^{TM} tubing was not

518   tested but Silonite^{TM}, which is believed to be a very similar product, was tested. The UCI WAS

519   uses SS canisters that are humidified, thus potentially mitigating absorptive losses on the canister

520   surfaces. The PFP glass flasks have been tested for long-term storage of VSLS in surface-air

521   samples collected under a wide variety of humidity levels and storage times and no issues have

522   been found for CH_2Cl_2 measurements. An alternative hypothesis to explain measurement

523   discrepancies is that TOGA had a sampling artifact at these low humidities and that the

524   canister/flask measurements are more accurate. The rational for this hypothesis is that

525   subtropical jets in the UTLS region inhibits the horizontal transport of tracers, leading to small

526   values measured by UCI WAS and PFP (Jesswein et al., 2022). One problem with this

527   hypothesis is that there would have to be a mechanism for artifact formation in the TOGA

528   analytical system that would result in higher CH_2Cl_2 and 1,2-DCA mixing ratios in this region

529   than were actually present and to date we have not seen evidence of artifact formation for this

530   species. Additionally, better correlation between the model and TOGA results increases the

531   likelihood of our first hypothesis.

532   **3.2. Cl-VSLS abundance in different field studies**

533   Cl-VSLS were also measured by TOGA during ORCAS and CONTRAST. These two missions

534   as well as the ATom-2 deployment occurred primarily during the month of February in different

535   years previous to ATom. The vertical profiles of CH_2Cl_2, $CHCl_3$, and C_2Cl_4 from ORCAS and

536   CONTRAST are also shown in
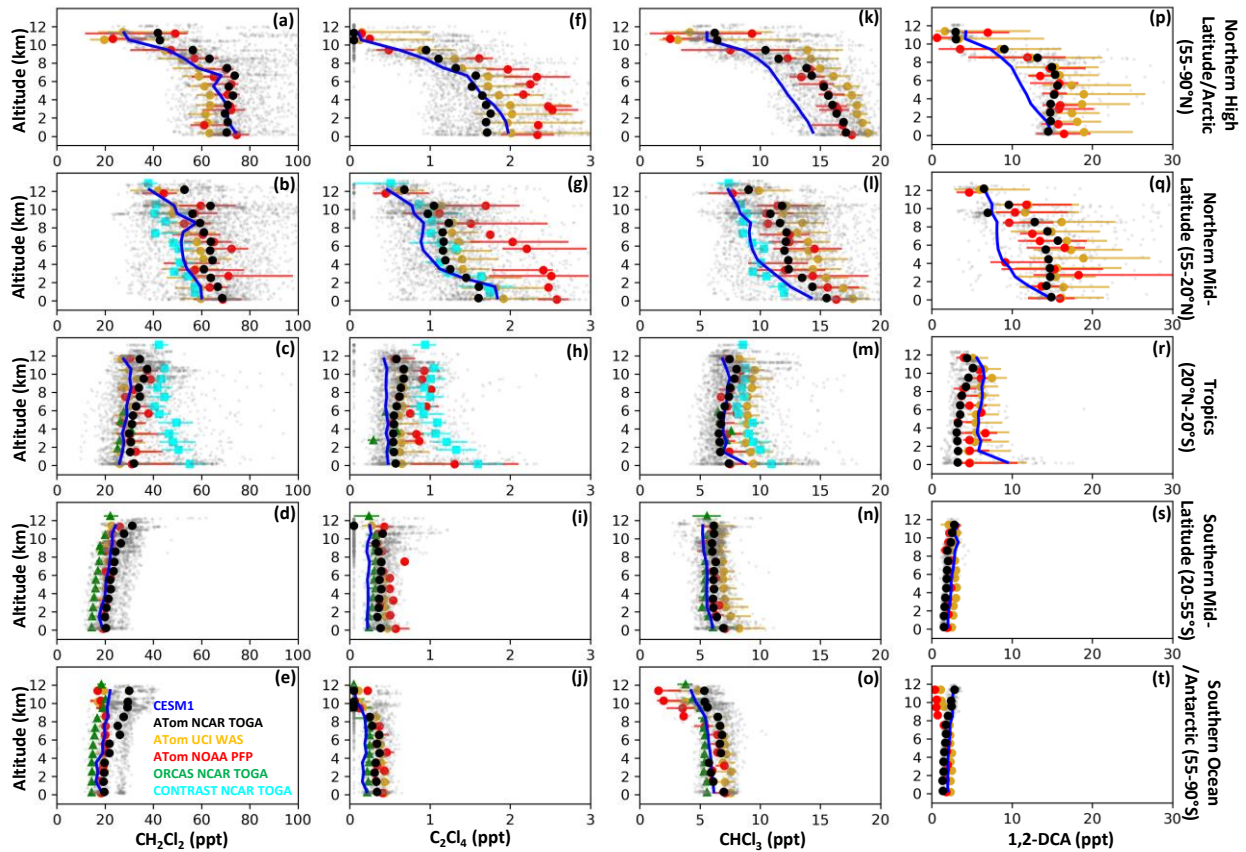
537

538   Figure **2** (and Figures S2-S4). Both ORCAS and ATom sampled air from similar regions in the

539   SH (Figure 1) but different years and the similar shape of the vertical profiles (in Figures S2-S4)

540   shows small interannual variability of the Cl-VSLS mixing ratios. On the other hand, the

541   CONTRAST mission sampled air masses in the western tropical Pacific region closer to Asia,

542   which led to higher mixing ratios compared with the ATom data (Figures S2-S4). In addition, the

543   vertical profiles for the CONTRAST Cl-VSLS had sharper gradients in the MBL compared with

544   ATom data, suggesting that low-level outflow from the Asian continent was sampled. Also, the

545   fast convection over the Pacific increases the Cl-VSLS levels at higher altitudes.

546   Figure 4 shows correlations of observed C_2Cl_4 vs. CH_2Cl_2 and $CHCl_3$ vs. CH_2Cl_2 for ORCAS,

547   CONTRAST, and ATom-2. It is worth mentioning that only ATom-2 is considered in this

548   analysis to match the seasons. C_2Cl_4 vs. CH_2Cl_2 for the ORCAS and CONTRAST regional

549   missions are overlaid on ATom-2 global data and show similar positive correlations. In

550   particular, the C_2Cl_4/CH_2Cl_2 ratio was 0.02 and 0.03 for the limited latitudinal-range ORCAS

551   (Southern Ocean region) and CONTRAST (tropics) data, respectively. The C_2Cl_4/CH_2Cl_2 ratio

552   for the global latitudinal-range ATom-2 data was 0.01-0.04, decreasing for SH latitude bins,

553   suggesting less transported C_2Cl_4 in the SH or faster loss in the SH. We will analyze

554   interhemispheric transport in more detail in Section 3.4. Figure 4 also shows similar tight

555   positive correlations between $CHCl_3$ and CH_2Cl_2 during CONTRAST and ATom-2 data, while

556     $CHCl_3$ does not correlate with CH_2Cl_2 in some of the ORCAS data. Within the Southern Ocean

557   region, this was also seen in the ATom-2 data (Figure S6). As shown in Figure 4d, there are two

558   clusters of data in the Southern Ocean/Antarctica latitude bins (55–90°S). One cluster contains

559   low CH_2Cl_2 and relatively high $CHCl_3$ mixing ratios that are measured near the surface. We

560   found positive correlation between near the surface $CHCl_3$ and two major oceanic tracers (CH_3I

561   and $CHBr_3$) during ORCAS, confirming the role of natural oceanic emissions of $CHCl_3$ in the

562   Antarctic region (not shown). In contrast, the other cluster shows a positive correlation between

563     $CHCl_3$ and CH_2Cl_2 at high altitudes. Since the lifetime of CH_2Cl_2 and $CHCl_3$ are of the same

564   magnitude (Hossaini et al., 2019), the positive correlation suggests this cluster is being

565   transported from other regions; i.e., from the NH or tropics. The natural sources of $CHCl_3$

566   include both oceanic (macro and microalgae) and terrestrial (soil) sources, with more natural

567   emissions in the NH than the SH (Laturnus et al., 2002). Nevertheless, the strong correlation

568   between $CHCl_3$ and CH_2Cl_2, in particular in the tropics and NH (Figure S6), also suggests that

569   maybe anthropogenic sources dominate $CHCl_3$ emissions sources. Fang et al. (2019) and An et

570   al. (2023) have shown that the changes in anthropogenic emissions can explain the recent

571   changes in global concentrations.
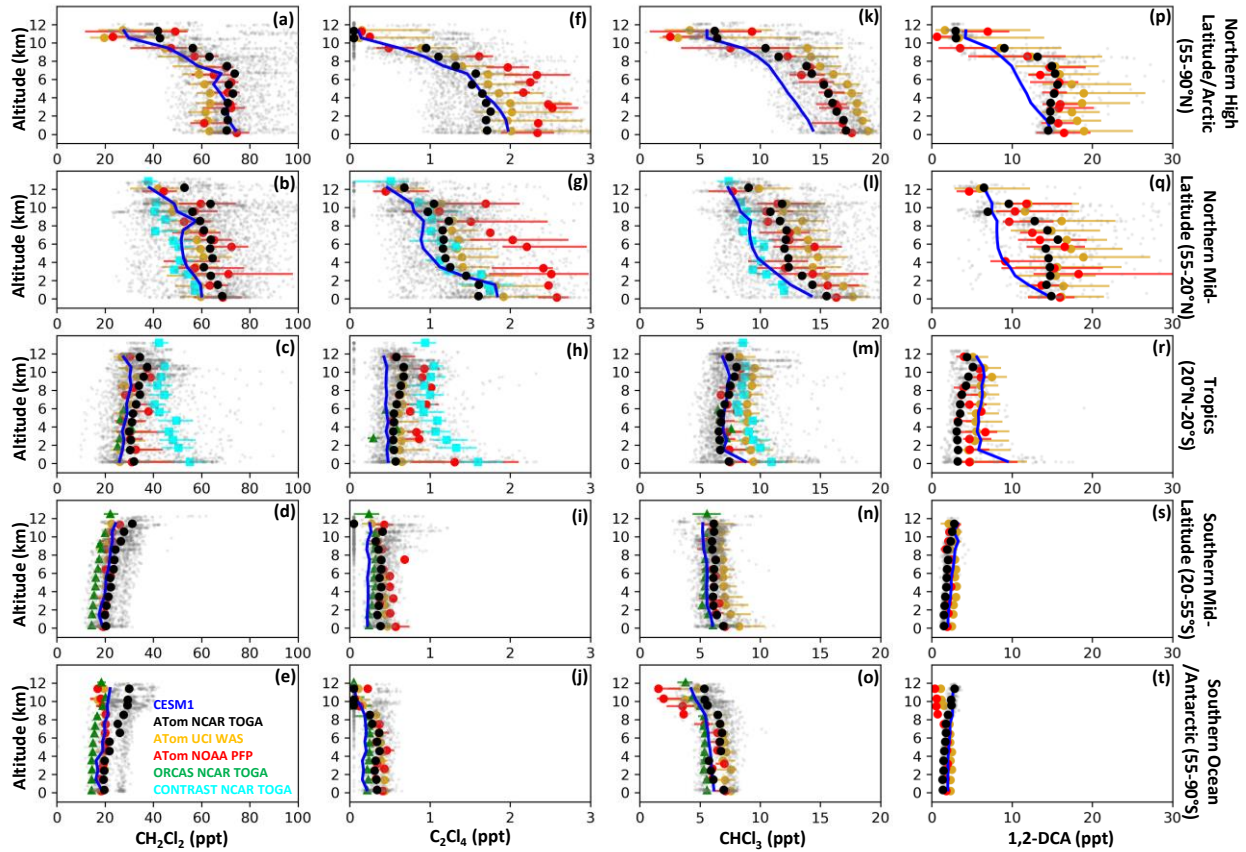
Figure 2. Binned vertical profiles of median measured CH_2Cl_2, C_2Cl_4, $CHCl_3$, and 1,2-DCA mixing ratios for all ATom deployments from TOGA (black), WAS (gold), and PFP (red), separated into five different latitude bins; 55–90°N (a, f, k, p), 20–55°N (b, g, l, q), 20°S–20°N (c, h, m, r), 55–20°S (d, i, n, s), and 90–55°S (e, j, o, t), accompanied by the vertically-binned median CESM1 model results sampled along the ATom flight tracks (blue curve). Note that C_2Cl_4 data for PFP (red points) are only available for ATom-4. Additionally, 1,2-DCA data for PFP are for ATom-2 to ATom-4 and for TOGA are only for ATom-4 – see Figures S2-S5 for individual deployments. Vertically-binned median TOGA measurements made during ORCAS (green) and CONTRAST (cyan) are also shown. Individual ATom TOGA data points are included (light grey points) although the *x*-axes are limited for better clarity in the SH plots. Error bars for PFP, WAS, CONTRAST, and ORCAS data are the 25th to 75th percentiles.
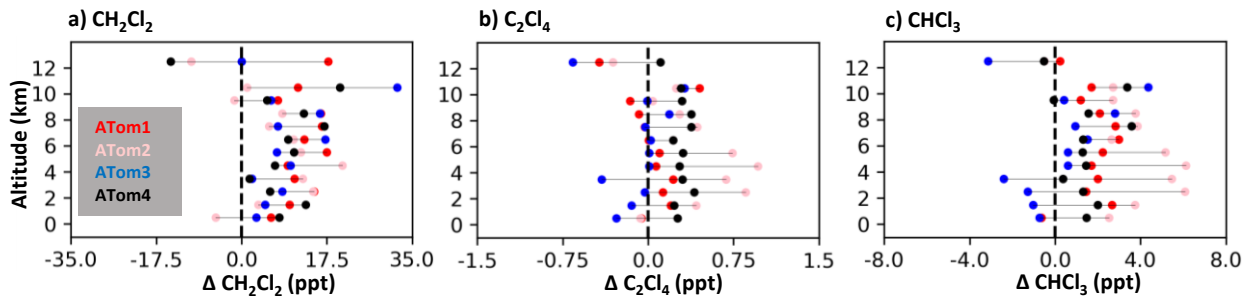
Figure 3. Vertical profiles of the median Pacific minus median Atlantic mixing ratios for (a) CH_2Cl_2, (b) C_2Cl_4, and (c) $CHCl_3$ from the TOGA observations at northern mid-latitudes (20–55°N). Marker colors show the differences during ATom-1 (red), ATom-2 (pink), ATom-3 (blue), and ATom-4 (black); negative values indicate that median

588   mixing ratios over the Atlantic were larger than the Pacific. Note the horizontal grey lines only connect the points
589   for better visualization and do not show the range of the observations.

590
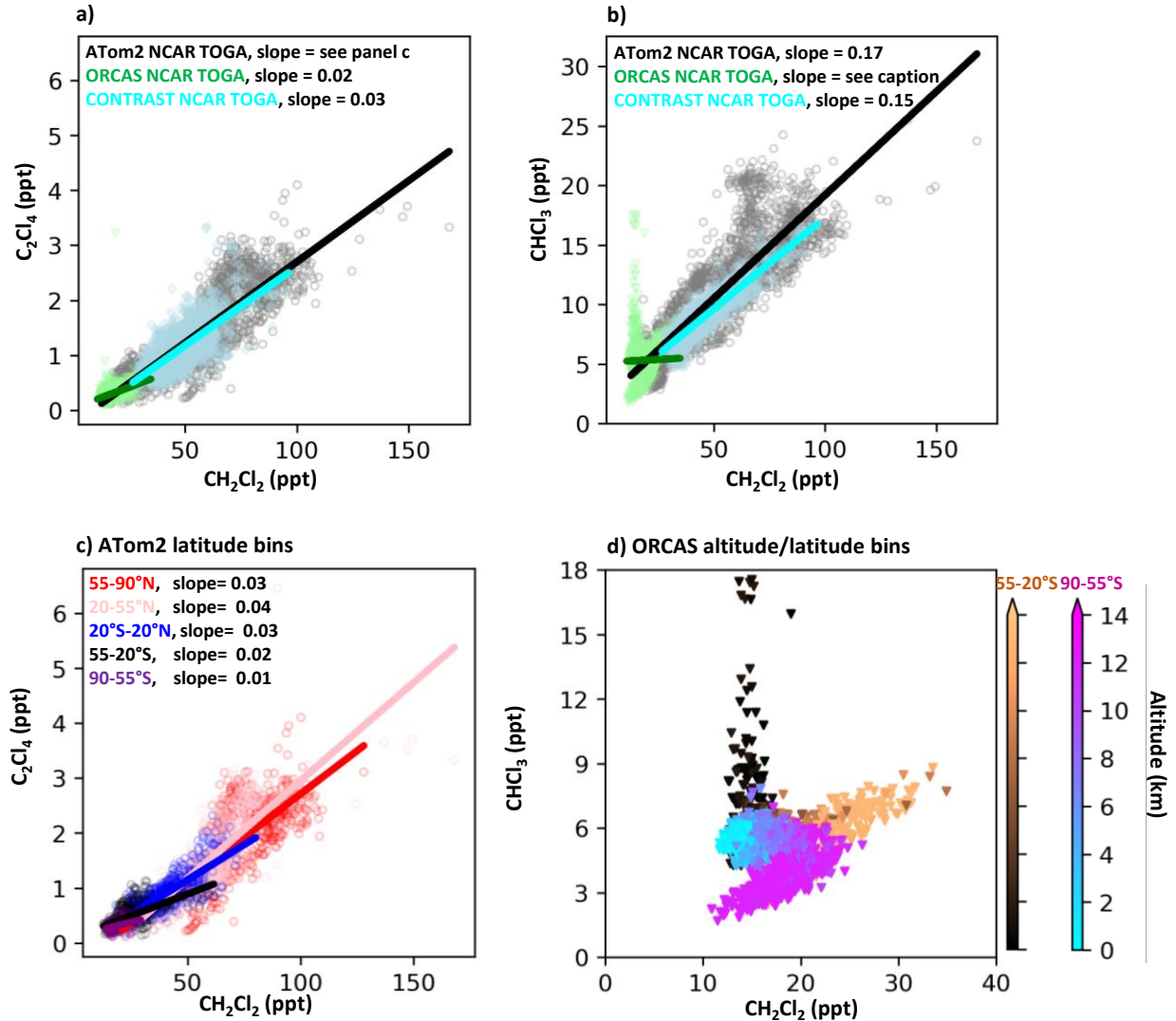
Figure 4. Correlation plots of Cl-VSLS measured by TOGA for (a) C_2Cl_4 vs. CH_2Cl_2 and (b) $CHCl_3$ vs. CH_2Cl_2
from ATom-2, ORCAS, and CONTRAST, (c) C_2Cl_4 vs. CH_2Cl_2 from ATom-2, colored by latitude bins, and (d)
$CHCl_3$ vs. CH_2Cl_2 from ORCAS colored by latitude bin and shaded by altitude. Lines show least square linear
regressions. Note that although a line is shown for $CHCl_3$ vs. CH_2Cl_2 from ORCAS in (b), regional data in (d)
indicate a non-linear relationship. Note that the axes are different in each panel. Note also that only ATom-2 data are
considered in this analysis to match the seasons with the CONTRAST and ORCAS projects.

3.3. Evaluation of CESM1 using ATom measurements
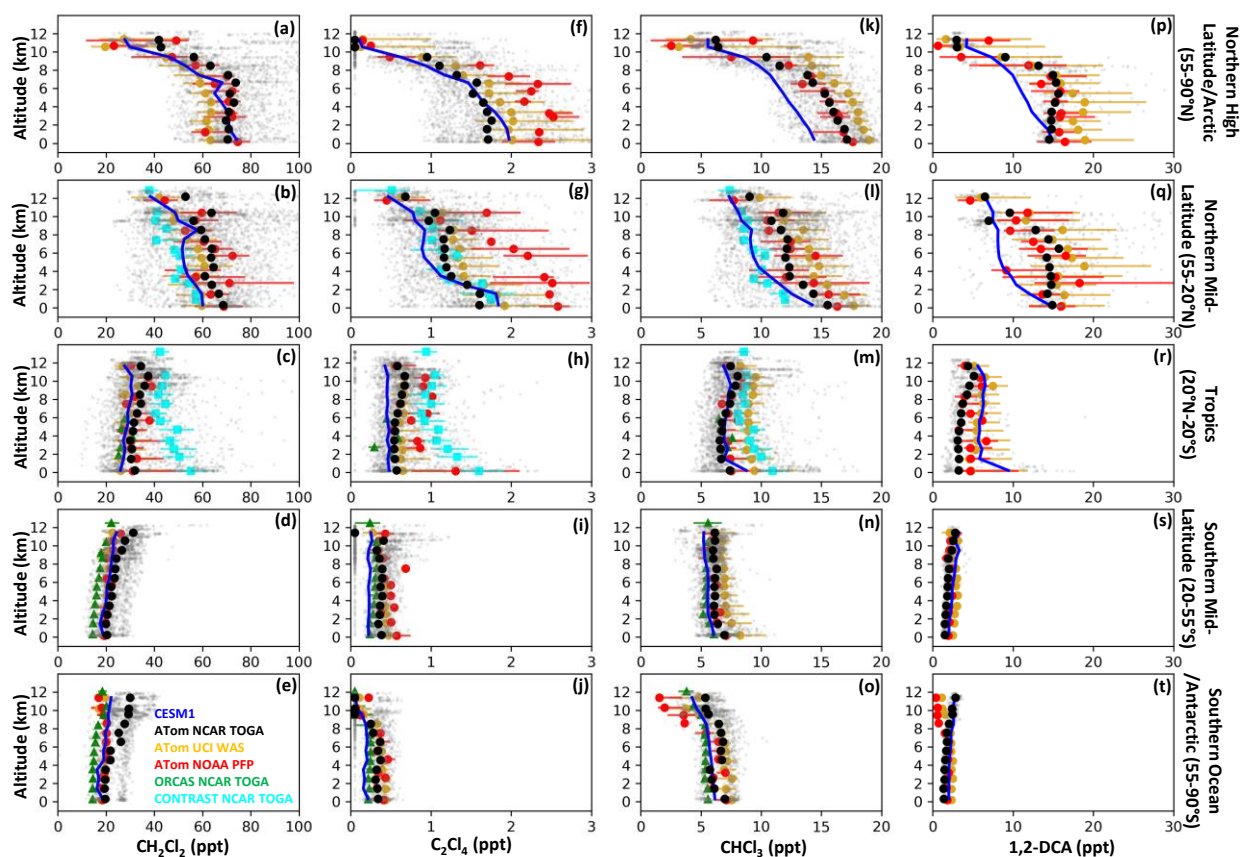
Figure 2 includes the vertical profiles of median modeled Cl-VSLS species in CESM sampled along ATom flight tracks and corresponding to TOGA measurement times. Similar to the measurements, the model showed substantially higher Cl-VSLS mixing ratios in the NH. For CH_2Cl_2, the model captured the observed vertical gradients; i.e., mixing ratios decreasing with increasing altitude in the NH and a slight vertical inversion (higher levels at higher altitudes) in the tropics and SH. The model captured the magnitude of the median surface layer (i.e., < 1 km) CH_2Cl_2 mixing ratios in the high-latitude Arctic region, but was approximately 10 ppt lower than the measurements in the northern mid-latitudes. In addition, the modeled CH_2Cl_2 mixing ratios were lower than TOGA measurements in the tropics and SH throughout the troposphere. Overall, we report the NMB, RMSE, and *r* of -15%, 16 ppt, and 0.80, respectively, for modeled CH_2Cl_2 against TOGA measurements in all ATom deployments (Table S4). For C_2Cl_4, the model captured the surface mixing ratios over the extratropical regions in the NH. However, the model was biased low at higher altitudes in the northern mid-latitudes. Additionally, the model was

612   biased low in the tropics and SH. The NMB, RMSE, and r for C_2Cl_4 are -7%, 0.5 ppt, and 0.82,

613   respectively (Table S5). Our model used constant LBC values, rather than emissions, for $CHCl_3$

614   and 1,2-DCA. For $CHCl_3$, the model underestimated the concentrations with NMB, RMSE, and r

615   of -17%, 3 ppt, and 0.85, respectively. Similarly for 1,2-DCA, the model underestimated its

616   global abundance with NMB, RMSE, and r of -23%, 6 ppt, and 0.74, respectively. (Note that

617   TOGA measured 1,2-DCA only during ATom-4). The model captured the Cl-VSLS mixing

618   ratios in the tropics and SH, with UCI WAS generally showing higher values than TOGA and

619   PFP. On the other hand, the model bias for $CHCl_3$ and 1,2-DCA was larger than CH_2Cl_2 and

620   C_2Cl_4 over the NH high latitudes. Statistics for individual ATom deployments are also listed in

621   Tables S4–S7. In the following sections, we look in more detail on model performance and

622   transport of CH_2Cl_2 and C_2Cl_4, which have anthropogenic sources with well-constrained

623   magnitudes (Claxton et al., 2020).

624   Figure 5 shows the measured and corresponding modeled profiles for CH_2Cl_2 and C_2Cl_4 mixing

625   ratios for each ATom deployment, binned zonally (Figure S7 shows similar plots for $CHCl_3$ and

626   1,2-DCA, as well as the OH observed by the Pennsylvania State University Airborne

627   Tropospheric Hydrogen Oxides Sensor, ATHOS). Both measurements and model output show

628   strong seasonal differences for Cl-VSLS in the NH. For CH_2Cl_2, both the highest measured and

629   modeled mixing ratios were over the NH high latitudes. However, the highest modeled values

630   were for ATom-4 (May 2018) but the highest measured values were during ATom-2 (February

631   2017). In the NH, CH_2Cl_2 up to 100 ppt was measured during ATom-3 (October 2017), yet the

632   model values only reached 60 ppt. Since the model is biased high for OH concentration (Figure

633   S7), and Cl-VSLS lifetimes are a few months, the large bias of the model during ATom-3 could

634   be due to the integrated impact of high-biased OH during the highest OH exposure period in the

635   NH. The lowest modeled CH_2Cl_2 mixing ratios in the NH were for the ATom-1 (August 2016)

636   period, consistent with the measurements. In addition, the model predicted a homogenous NH

637   vertical gradient during ATom-1, which is also consistent with the measurements. For C_2Cl_4,

638   both model and measurements agreed with the highest NH mixing ratios during ATom-2

639   (February 2017), although the model overestimates the mixing ratios (NMB of 24% in high-

640   latitude Arctic region). Similar to CH_2Cl_2, the lowest NH C_2Cl_4 mixing ratios were during

641   ATom-1, both measured and modeled. The high mixing ratios during ATom-2 (February 2017)

642   and low mixing ratios during ATom-1 (August 2016) reveal seasonal differences for both

643 CH_2Cl_2 and C_2Cl_4, which the model clearly captured. This seasonal variation can be explained

644 primarily by OH seasonal variations, as the emissions in the model were constant throughout the

645 year (Figure S7). In particular, lower [OH] during NH winter leads to greater Cl-VSLS

646 abundance, with the opposite true in NH summer. In addition, atmospheric dynamics play a role

647 in the observed mixing ratios. For example, the enhanced high-altitude Cl-VSLS mixing ratios

648 measured in the NH mid-latitudes during ATom-1 are potentially due to the Asian Summer

649 Monsoon deep convection. Wang et al. (2020) found that the CAM-chem model captured the

650 large-scale processes during ATom-1 and ATom-2 including the isentropic mixing from low

651 latitudes to high latitudes. Similar to Wang et al. (2020), the wind fields and temperature in the

652 model in this work are nudged towards the MERRA-2 reanalysis data to better capture the large-

653 scale processes.

654
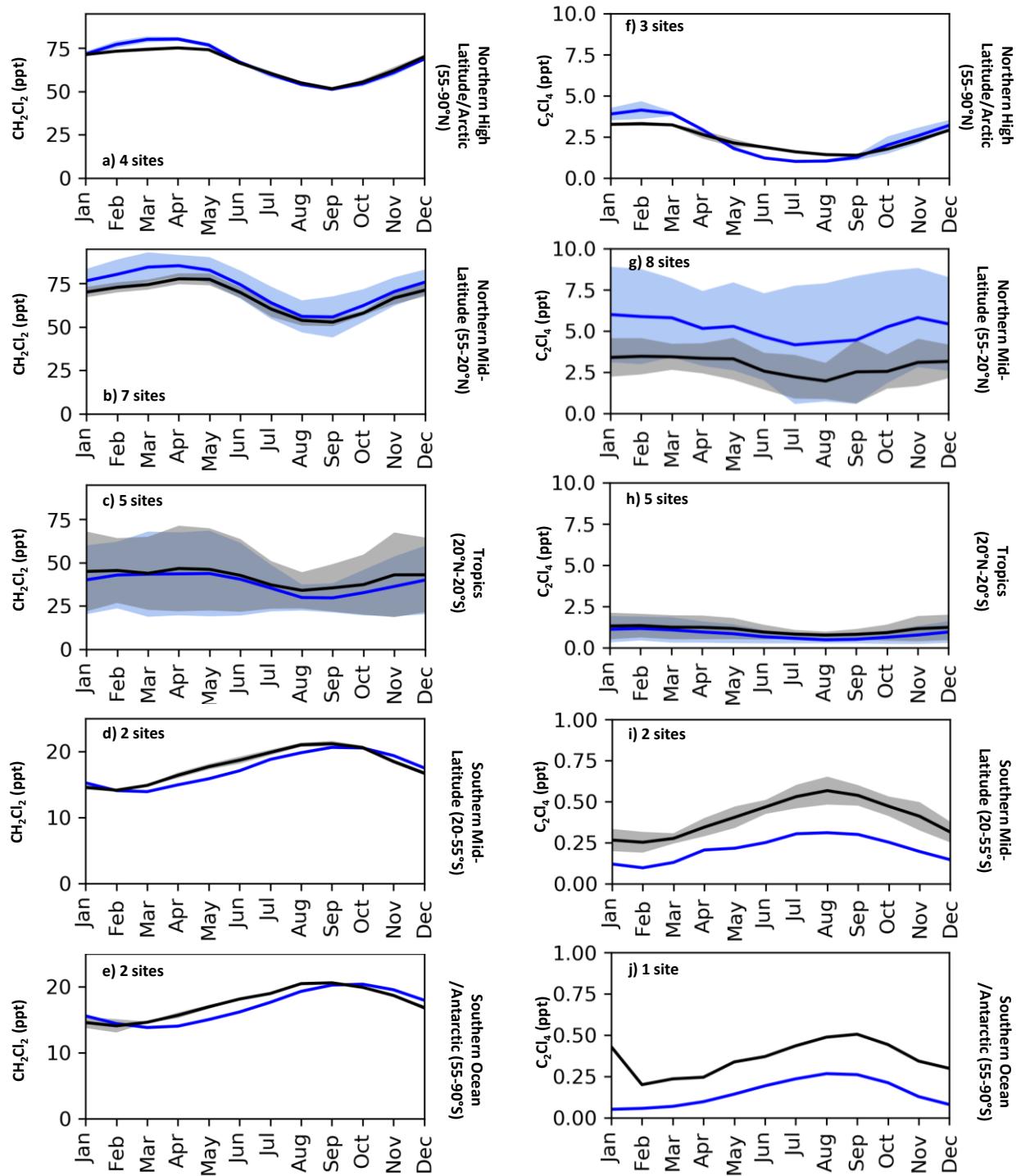
Figure **6** shows the monthly means of surface CH_2Cl_2 and C_2Cl_4 mixing ratios modeled and

observed by ground measurement stations between 2016 and 2018 and using the corresponding

model grid cells, divided into latitude bins. For CH_2Cl_2, the model overestimated the maximum

in the observations in NH mid-latitudes during winter and spring and captured the minimum

659   values during summer, and measurements were in the range of modeled data. Over other regions,

660   the model mostly underestimated the CH_2Cl_2 mixing ratios. The majority of stations were located

661   in the tropics (five stations) and northern mid-latitudes (seven stations), where the spread of

662   modeled and observed values overlapped with each other. The NMB, RMSE, and *r* for monthly

663   mean CH_2Cl_2 data against all ground measurement data are 2%, 8 ppt, and 0.95, respectively. It

664   should be noted that over the SH regions, the model minimum and maximum values are delayed

665   (by about 1 month) for CH_2Cl_2 compared to the measurements, while the model more accurately

666   predicts the timing of the maximum and minimum values of C_2Cl_4. This delay difference can be

667   explained by different source regions for CH_2Cl_2 and C_2Cl_4. In particular, Asian emission

668   dominate SH abundance of CH_2Cl_2, while C_2Cl_4 abundance are attributed more evenly to

669   regions, as will be discussed in Section 3.4. For C_2Cl_4, the model captured the maximum values

670   in the high-latitude Arctic region. In the northern mid-latitudes, a less pronounced seasonal

671   variability was observed, which was captured by the model, despite being always biased high

672   and with a larger standard deviation. Similar to CH_2Cl_2, the model is biased low for C_2Cl_4 in the

673   tropics and Southern Hemisphere. The NMB, RMSE, and *r* of 45%, 2 ppt, and 0.79, respectively,

674   show the overestimation of C_2Cl_4. This is in contrast with the model being biased low, in

675   general, against ATom data as mentioned above (NMB of -7%). The overestimation during all

676   the months over the NH mid-latitudes and strong underestimation in the SH (i.e., emission

677   sources) suggests either C_2Cl_4 emission magnitudes or global distributions require further

678   improvements.

679

680
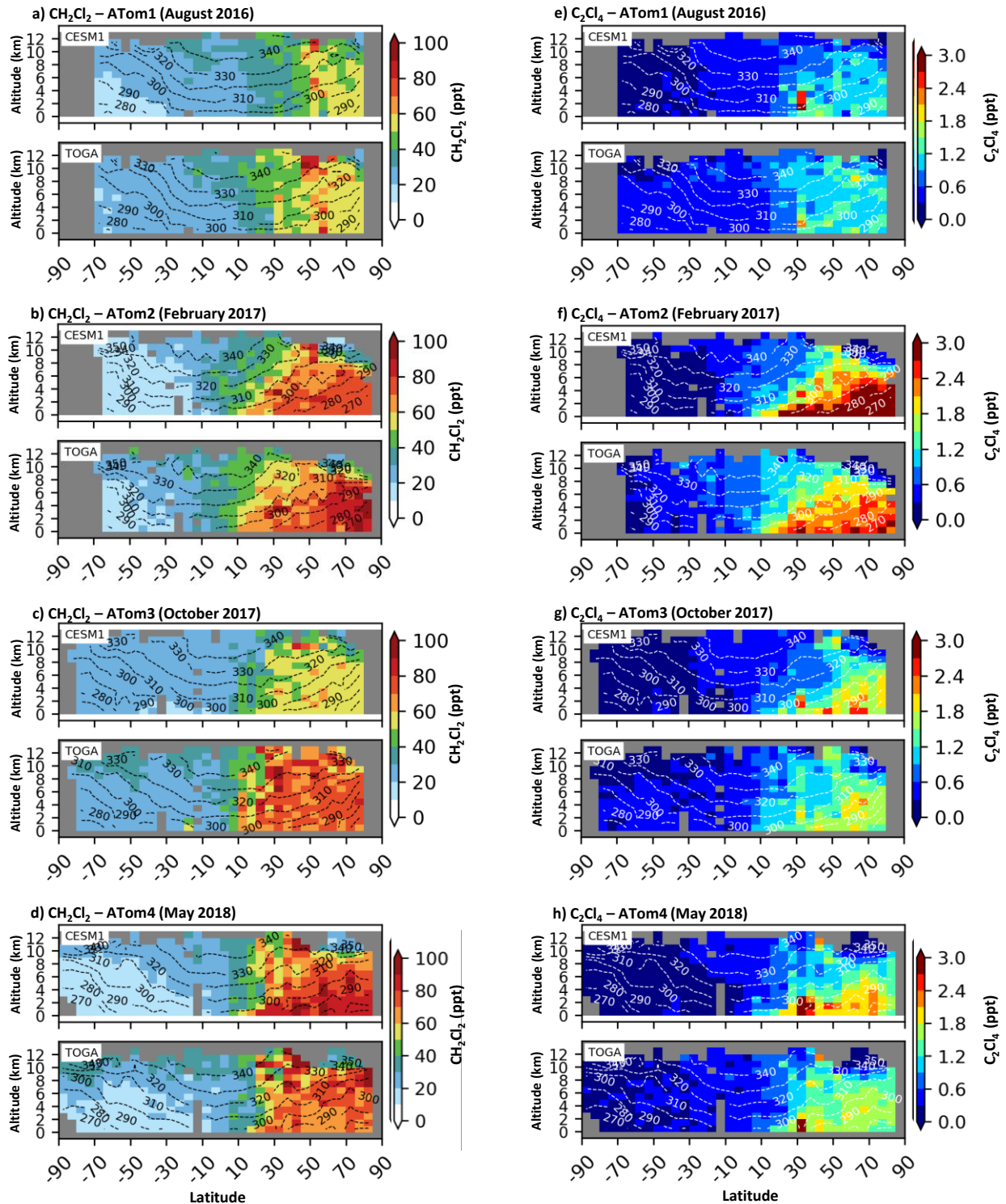
Figure 5. Spatially-binned distribution of mean modeled (top subplot) and measured (bottom subplot) for (a-d) CH_2Cl_2 and (e-h) C_2Cl_4 mixing ratios during individual ATom deployments. Latitude and altitude bin intervals are 5 degrees and 1 km, respectively. Corresponding TOGA sample locations for each ATom mission are shown in Figure S7.

685 **Table 2**. Summary of TOGA-observed median mole fractions (and 10th–90th percentiles) for four Cl-VSLS and total
686 Cl^{VSLS} during ATom within different latitude and altitude bins.

Latitude Region	Potential Temperature θ (K)	CH_2Cl_2[a], ppt	C_2Cl_4[a], ppt	$CHCl_3$[a], ppt	1,2-DCA[b], ppt	Σ Cl^{VSLS} [c], ppt
Northern High Latitudes/ Arctic	< 320	70.2 (54.1 - 91.6)	1.5 (1.0 - 2.4)	15.3 (11.4 - 18.7)	14.8 (12.6 - 18.2)	206.4 (150.0 - 251.2)
	320-340	59.4 (41.3 - 94.7)	1.1 (LLOD - 1.60)	11.4 (6.6 - 15.3)	11.1 (4.0 - 15.9)	166.1 (105.0 - 244.3)
	340-360	33.8 (25.9 - 46.3)	LLOD	5.2 (4.2 - 6.6)	2.9 (2.4 - 4.1)	86.7 (66.8 - 119)
	360-380	41.6 (33.1 - 57.5)	LLOD	5.8 (4.8 - 8.1)	3.1 (2.5 - 3.4)	106.6 (85.3 - 139.3)
Northern Mid-latitudes	< 320	66.2 (45.4 - 81.7)	1.4 (0.8 - 2.3)	14. (9.2 - 17.9)	14.7 (9.8 - 20.5)	189.9 (129.2 - 234.1)
	320-340	59.2 (39.7 - 96)	1.1 (0.6 - 1.6)	11.5 (7.8 - 15.2)	11.7 (5.7 - 27.4)	162.9 (107.2 - 258.7)
	340-360	41.6 (34.2 - 67.3)	0.7 (LLOD - 1.1)	8.3 (6.7 - 10.6)	6.5 (3.5 - 16.5)	110.8 (93.6 - 171.5)
	360-380	N.A.[d]	N.A.	N.A.	N.A.	N.A.
Tropics	< 320	31.1 (21.1 - 59.5)	0.6 (0.3 - 1.4)	7.1 (5.5 - 12.3)	3.3 (1.8 - 11.3)	86.4 (63.7 - 166.3)
	320-340	33.2 (23.4 - 48)	0.6 (0.4 - 1.0)	7.2 (5.8 - 9.8)	3.6 (2.5 - 6.6)	91.7 (69.5 - 130.2)
	340-360	35.7 (27.3 - 47.5)	0.6 (0.4 - 0.9)	7.7 (6.3 - 10.0)	4.8 (2.9 - 5.7)	99.6 (76.7 - 130.5)
	360-380	N.A.	N.A.	N.A.	N.A.	N.A.
Southern Mid-latitudes	< 320	21.9 (16.1 - 28.7)	0.4 (LLOD - 0.51)	6.3 (5.1 - 7.6)	1.7 (1.3 - 2.1)	65.2 (51.9 - 80.4)
	320-340	27.4 (20.8 - 33.6)	0.4 (LLOD - 0.6)	6.0 (4.6 - 6.9)	2.5 (2.0 - 3.0)	75.9 (58.8 - 88.8)
	340-360	30.5 (22.7 - 39.7)	0.5 (LLOD - 0.8)	6.1 (4.3 - 7.6)	3.2 (2.9 - 3.4)	81.2 (61.2 - 102.2)
	360-380	25.6 (22.4 - 27.9)	LLOD	3.6 (3.2 - 4.7)	N.A.	61.5 (55.5 - 70.2)
Southern Ocean/ Antarctic	< 320	24.8 (16.7 - 30.8)	0.3 (LLOD - 0.5)	6.5 (5.1 - 7.7)	1.6 (1.3 - 2.3)	71.2 (51.4 - 83.9)
	320-340	29.1 (22.5 - 35.5)	LLOD (LLOD - 0.4)	5.3 (3.8 - 5.9)	2.4 (2.0 - 2.9)	76.7 (58.8 - 91.1)
	340-360	34.2 (23.4 - 39.5)	LLOD	4.9 (3.5 - 6.0)	2.8 (2.3 - 3.2)	87.6 (57.5 - 102.5)
	360-380	29.3 (24.3 - 39.9)	LLOD	4.6 (3.3 - 5.9)	3.0 (2.3 - 3.4)	73.4 (60.2 - 104.9)

687 [a] The reported values for CH_2Cl_2, C_2Cl_4, and $CHCl_3$ are based on TOGA data for all ATom deployments.
688 [b] 1,2-DCA is only available from TOGA for ATom-4.
689 [c] Total Cl atoms from the sum of available chlorine in CH_2Cl_2, $CHCl_3$, C_2Cl_4, and 1,2-DCA.
690 [d] N.A. = data not available.
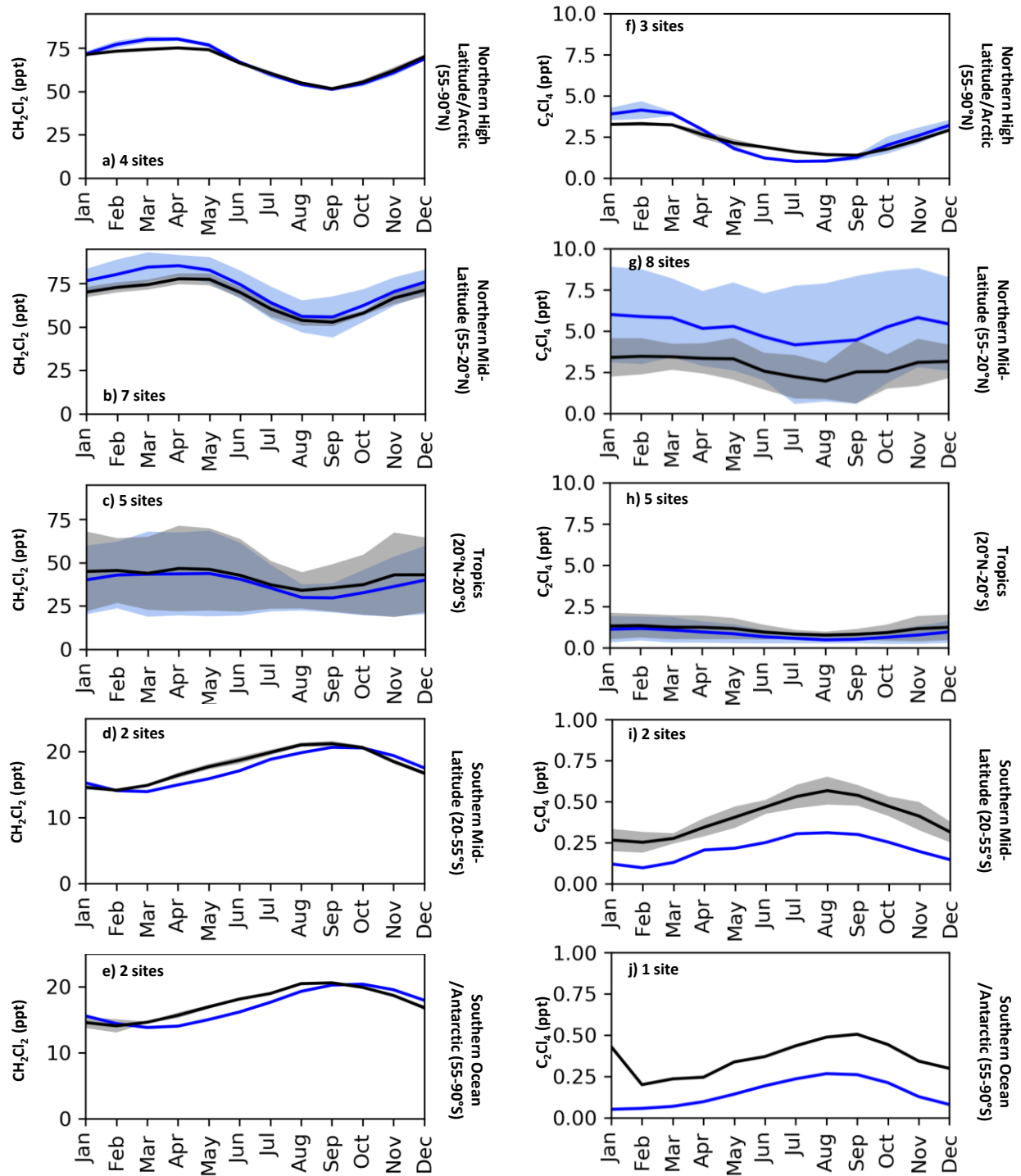
Figure 6. 2016–2018 monthly means of ground-based measurements (black) and corresponding modeled (blue) ± 1 standard deviation (shading) of CH_2Cl_2 and C_2Cl_4 mixing ratios over five different latitude bins: 55–90°N, 20–55°N, 20°S–20°N, 55–20°S, and 90–55°S. Ground-based measurements are from the stations within NOAA and AGAGE networks shown in Figure 1. The shading represents the ± 1 standard deviation of the monthly means from multiple sites within each latitude range and not the spread over different years for individual sites. Note that for many months the standard deviations (both model and measurements) are very small compared with the *y*-axes scales. Also, note that smaller *y*-axes limits are used for SH panels.

699 **3.4. Impact of transport and convection from regionally tagged emissions of Cl-VSLS**

700   As shown in the previous sections, the model was mostly able to capture the distribution and

701   seasonal variability of four Cl-VSLS. We also observed the presence of these Cl-VSLS in the SH

702   remote regions and high altitudes despite the fact that the large majority of their emissions are in

703   the NH. In this section, we use the regional tagged tracers (described in Section 2.2.2) to estimate

704   the contribution of emissions from each region on Cl-VSLS abundance at various altitudes and

705   locations.

706   Figure 7 shows the spatial distribution of each regional tagged CH_2Cl_2 tracer at 950 hPa and 150

707   hPa during August 2017. The deep convection during August 2017 due to the Asian summer

708   monsoon (ASM) has been previously shown (Honomichl and Pan, 2020). Near the surface (i.e.,

709   950 hPa), the highest mixing ratios are near the source regions for the Asian (AS) and European

710   (EU) tagged tracers. The AS emissions are also the major contributor to the CH_2Cl_2 mixing ratios

711   over North America, South America, and Africa. Similarly, the AS emissions are the dominant

712   source of CH_2Cl_2 over the remote regions from the Arctic to the Antarctic (Figure 7a). In

713   addition, the NH mixing ratios over the high latitude regions that are contributed by the AS

714   region are larger than the mid-latitude regions. At high altitudes (i.e., 150 hPa), the AS emissions

715   are the dominant contributor around the globe (Figure 7e). In particular, AS mixing ratios above

716   50 ppt were modeled over their source regions in contrast with < 9 ppt mixing ratios from EU.

717   Furthermore, the model shows larger values at high altitudes than at the surface in the tropics and

718   subtropical regions in SH (Figure 7e). Figure 8, on the other hand, shows that AS, EU, and NA

719   emissions are the dominant contributors of C_2Cl_4 in their source regions and their impact on

720   other regions in the NH, near the surface, are within the same order. However, their contribution

721   in the SH is minimal compared to the cumulative impact of sources in the SH (Figure 8d). At

722   high altitudes, Asia is the dominant contributor to C_2Cl_4, and its impact is primarily limited to the

723   tropical regions. Adcock et al. (2021) and Lauther et al. (2022) showed that the ASM anticyclone

724   transports large amounts of surface Cl-VSLS emissions to the UTLS region, where they can be

725   transported horizontally by jet streams to other regions.

726   Figure 9 and 10 show the annual zonal means of the total and tagged emissions of CH_2Cl_2 and

727   C_2Cl_4, respectively, between 2016 and 2018. For CH_2Cl_2, we estimate the annual mean

728   tropospheric mixing ratios of 36.9 ppt (i.e., 73.8 ppt Cl), with the Asian emissions being

729   responsible for 85% of the total. Within Asia, we further calculated that China's annual mean

730   tropospheric mixing ratio of CH_2Cl_2 is 17.1 ppt, which accounts for 46% of global tropospheric

731   mean abundance. On continental scale, EU (8%) and NA (4%) emissions ranked second and

732   third as sources of tropospheric CH_2Cl_2, respectively. Table 3 shows the mean tropospheric

733   values in individual latitude bins, highlighting that AS emissions dominate in all regions.

734   Similarly, the vertical profiles of tagged emissions along the ATom flight tracks confirm the AS

735   dominance (Figure S8). For C_2Cl_4, in contrast, emissions from EU, NA, and AS are all important

736   contributors to the global annual mean tropospheric mixing ratio of 0.73 ppt (i.e., 2.92 ppt Cl).

737   The modeling results show that total chlorine from CH_2Cl_2 is ≈ 25 times more than from C_2Cl_4 in

738   the troposphere. The similar source gas ratio for TOGA measurements along the ATom flight

739   tracks is ≈ 28 (using 46.6 and 0.84 ppt global means of CH_2Cl_2 and C_2Cl_4, respectively, in

740   Section 3.1.5).

741   EU, NA, and AS contribute 32% (0.23 ppt), 27% (0.20 ppt), and 33% (0.24 ppt) to the global

742   mean C_2Cl_4, respectively. As Figure 10 shows, the C_2Cl_4 mixing ratios are highest over their

743   individual source regions with very low values in other regions, due to its shorter atmospheric

744   lifetime, which we will discuss in Section 3.5. While AF and SA C_2Cl_4 emissions do not strongly

745   impact global concentrations, the tagged zonal plots shows clear sensitivity of the C_2Cl_4

746   distribution to regional sources. In particular, Figure 10 suggests that an increase in future AF

747   and SA emissions could have a more significant impact than other continental sources on the SH

748   region, although an increase in C_2Cl_4 emissions is not anticipated based on current emission and

749   concentration trends (Claxton et al., 2020; Laube et al., 2022). Figures 9 and 10 also show

750   contributions from SA and AF over the tropics, and highlights the significance of the emission

751   regions. This is important as these regions become increasingly industrialized. This could lead to

752   more widespread use of VSLS in the future, which could be transported to the stratosphere and

753   impact the stratospheric ozone layer (Oram et al., 2017). The tagged emissions along the ATom

754   flight tracks for C_2Cl_4 also show relatively higher contribution of AF and SA emissions in the SH
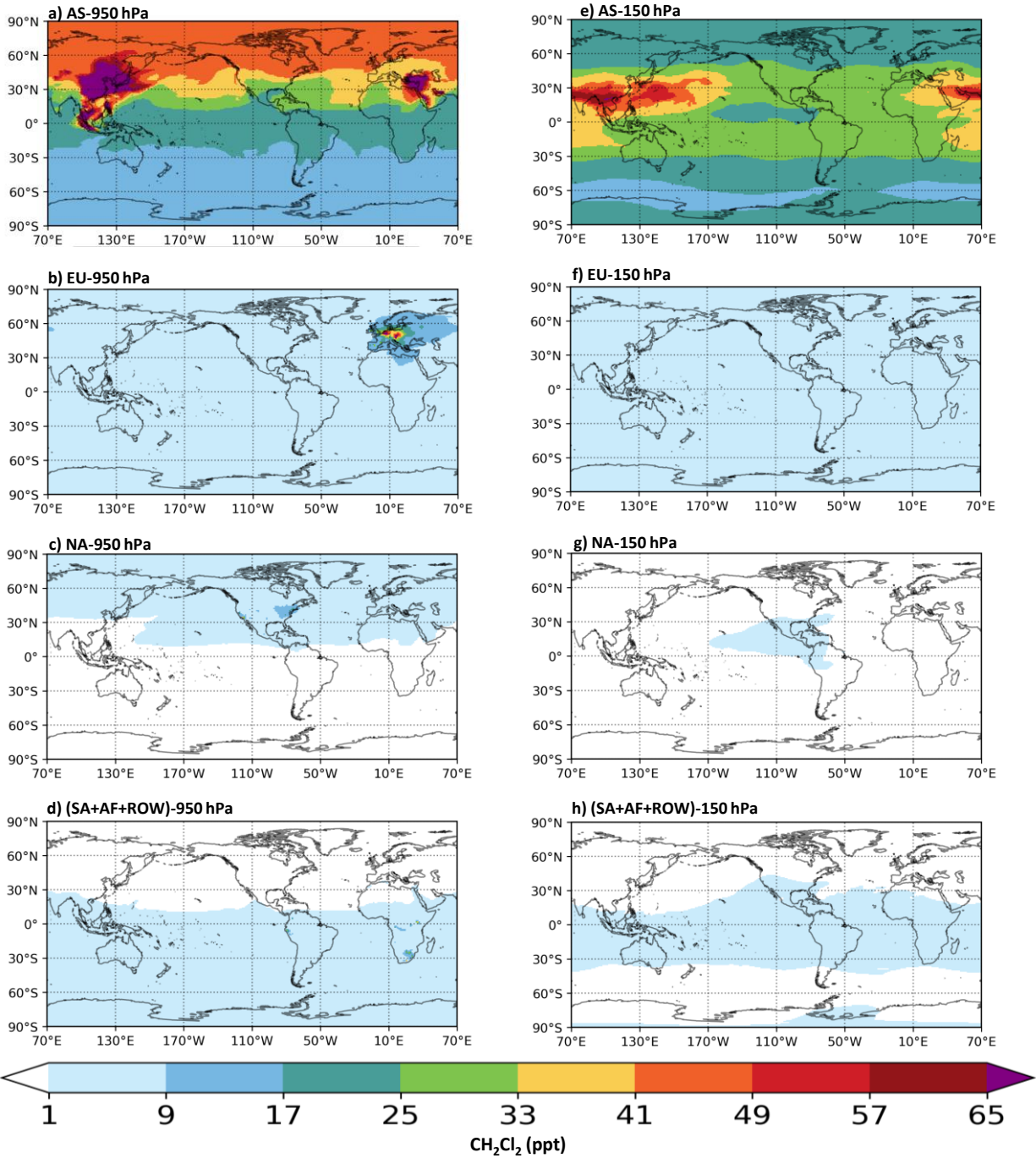
755   (Figure S9).

Figure 7. Maps of August 2017 mean CH_2Cl_2 mixing ratios of tagged emissions near the surface (950 hPa) and UTLS (150 hPa ≈ 13 km). AS: Asia, EU: Europe, NA: North America, SA: South America, AF: Africa, and ROW: Rest of the world.
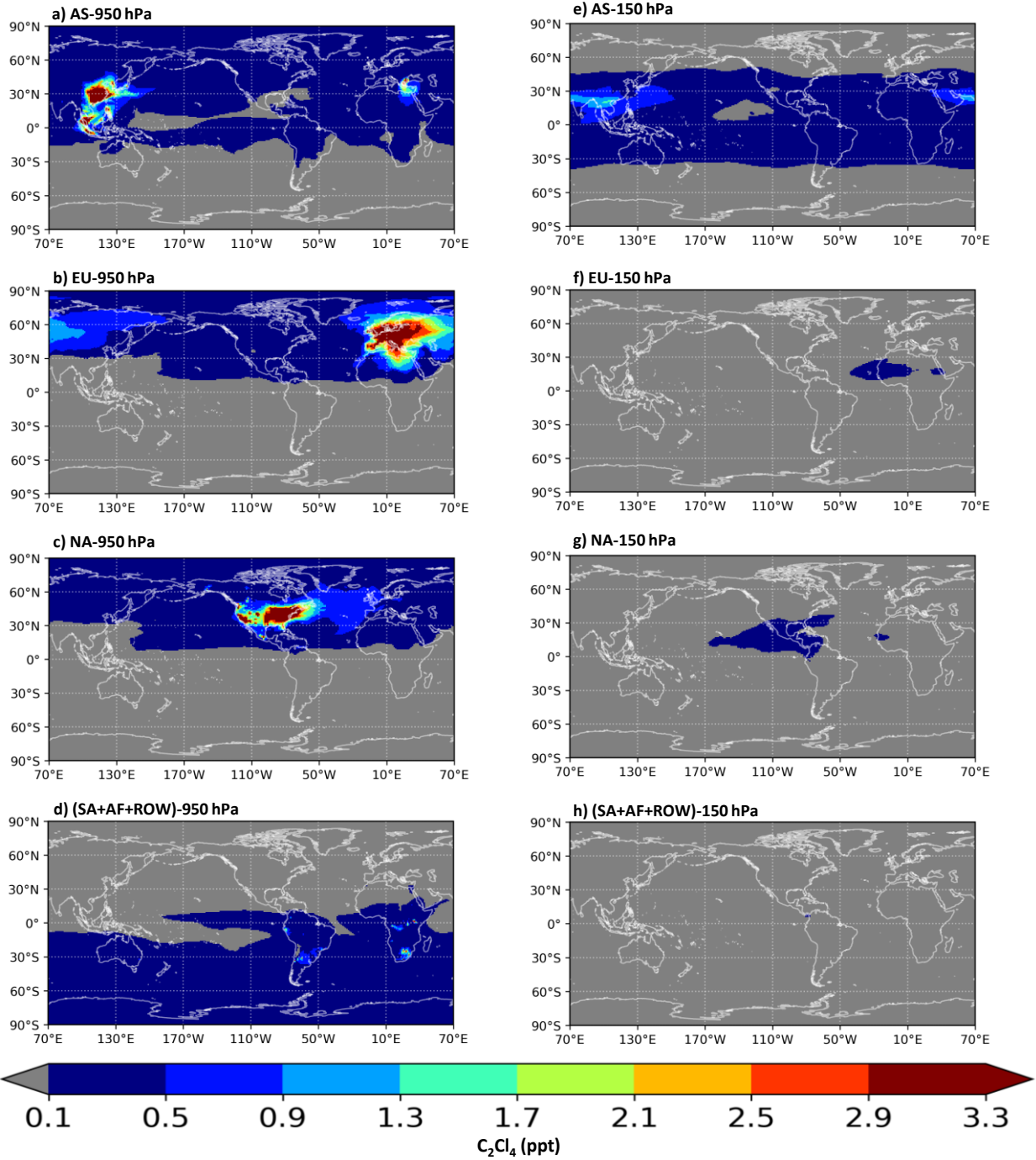
Figure 8. Same as Figure 7, but for C_2Cl_4. Note that all the values in (h) are below 0.1 ppt.
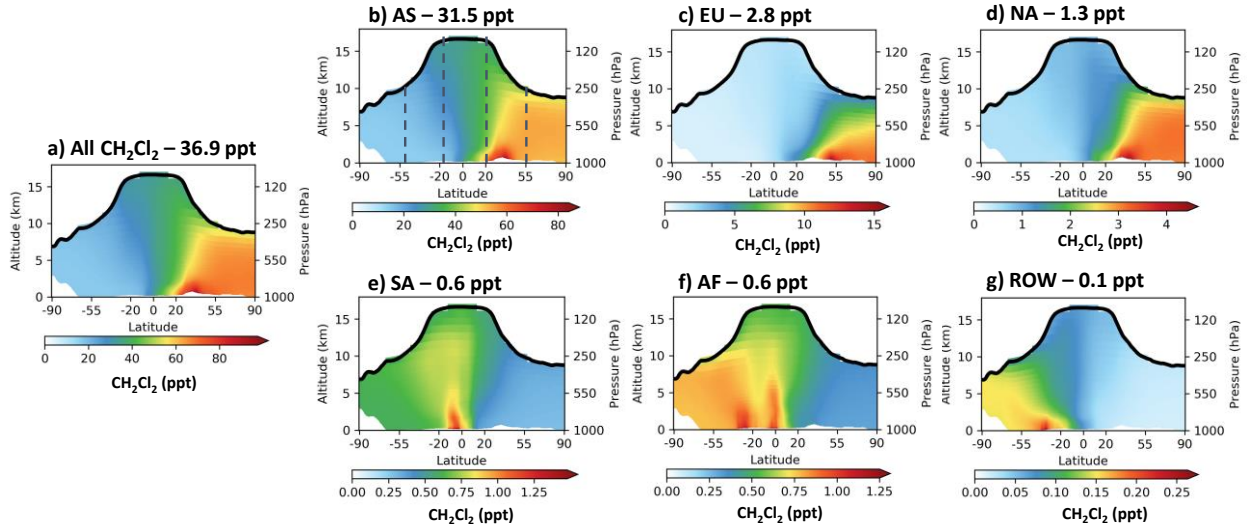
Figure 9. Modeled zonal 2016–2018 annual mean mixing ratios of (a) CH_2Cl_2 and (b-g) zonal mixing ratios resulting from tagged CH_2Cl_2 emissions from each designated region. The solid line shows the location of the mean modeled tropopause. The global tropospheric mean mixing ratios of the (a) global and (b-g) regionally-sourced CH_2Cl_2 are shown on top of each panel, where AS: Asia, EU: Europe, NA: North America, SA: South America, AF: Africa, and ROW: Rest of the world. The dashed line on (b) shows the latitudinal bins used in Table 3. Note that the color scales are different in each panel.
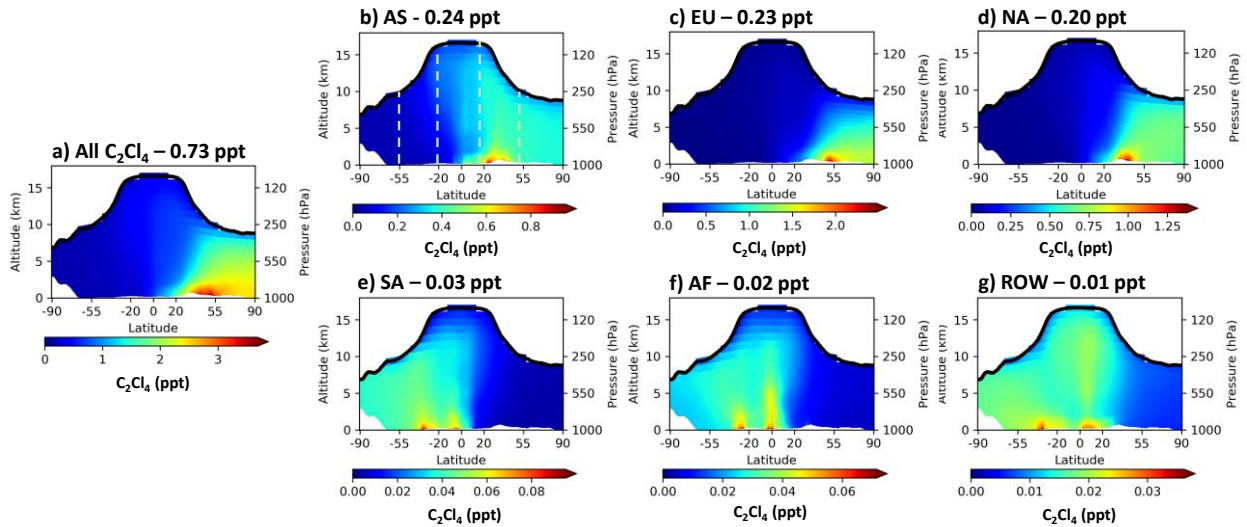
Figure 10. Same as Figure 9, but for C_2Cl_4.

773   **Table 3**. The annual mean (2016–2018) modeled tropospheric source contribution of CH_2Cl_2 and C_2Cl_4, in ppt, due
774   to tagged emissions in each source region.

Species	Region	Asia (China)	Europe	North America	South America	Africa	Rest of the World
CH_2Cl_2	High latitudes/ Arctic	52.90 (31.95)	7.98	2.92	0.32	0.33	0.02
	Northern mid-latitudes	46.69 (28.39)	4.33	2.05	0.41	0.42	0.03
	Tropics	28.86 (14.13)	1.86	1.02	0.71	0.65	0.06
	Southern mid-latitudes	18.38 (8.41)	1.16	0.65	0.69	0.76	0.11
	Southern Ocean/Antarctic	14.74 (6.74)	0.96	0.54	0.62	0.78	0.14
C_2Cl_4	High latitudes/ Arctic	0.36 (0.20)	0.94	0.62	0.004	0.005	0.007
	Northern mid-latitudes	0.39 (0.23)	0.42	0.40	0.01	0.01	0.01
	Tropics	0.26 (0.09)	0.10	0.11	0.03	0.03	0.02
	Southern mid-latitudes	0.10 (0.03)	0.03	0.03	0.04	0.03	0.02
	Southern Ocean/Antarctic	0.05 (0.01)	0.02	0.02	0.04	0.02	0.02

775   **3.5. Modeled major photochemical destruction pathways for Cl-VSLS**

776   Reactions with the OH radical, Cl atoms, and photolysis are known photochemical destruction

777   pathways of Cl-VSLS in the atmosphere and are included in the model (R1–R12). Figure 11

778   shows the mean rate of CH_2Cl_2 and C_2Cl_4 destruction via these reactions in different latitude bins

779   between 2016 and 2018. For CH_2Cl_2, reaction with OH is the dominant destruction pathway in

780   all latitude bins and within the vertical profile. Specifically, the OH reaction rate is 0.9–1.3

781   orders of magnitude higher than the Cl reaction rate. In addition, photolysis plays a significant

782   role only during summer and at high altitudes. Specifically, over the SH mid-latitudes and in the

783   tropics, the mixing ratios of CH_2Cl_2 and C_2Cl_4 decrease at a faster rate with increasing altitude

784   (sharper gradient) when photolysis (blue line) begins to compete with the Cl reaction.

785   As was shown in
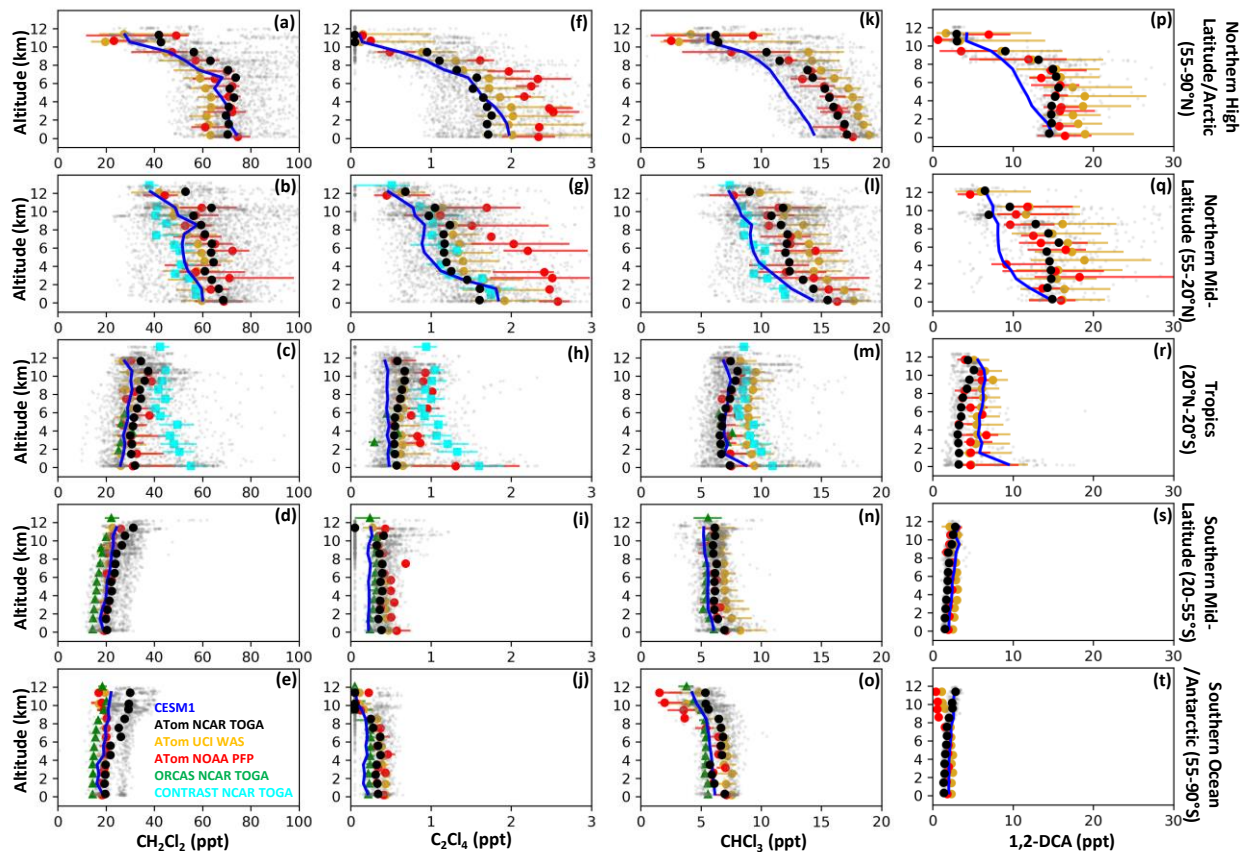
786

787   Figure **2**, the model underestimates CH_2Cl_2 mixing ratios. Reaction with OH is the main

788   destruction process of CH_2Cl_2. As OH is calculated online in the model, it is challenging to

789   separate the drivers of the sources and sinks of OH, thus the methane lifetime is a good indicator

790   of the average OH concentration. In our base simulation, the lifetime of methane was 8.4 years,

791   which is close to the reported values by other studies using CESM1 model (Tilmes et al., 2015;

792   Tilmes et al., 2016; Nicely et al., 2020), but lower than observational estimates (Prather et al.,

793   2012). Our model includes halogen chemistry, which has shown to increase the methane lifetime

794   by 6–9% (Li et al., 2022). Therefore, the uncertainties in the modeled OH (Stevenson et al.,

795   2020) could explain the bias in part for CH_2Cl_2. To investigate the OH sensitivity of the model

796   without directly attempting to change the OH amounts, we ran a simulation in which we reduced

797   the rate constant k_{OH} for all four Cl-VSLS (i.e., R2, R5, R8, and R11) by 10%, which decreased

798   the model bias for CH_2Cl_2 by 7% (Figure S10). It is shown that the modeled OH is not more than

799   ~10% too high (Stevenson et al., 2020), indicating the Cl-VSLS emissions inventories are likely

800   too low based on the persistent bias with the adjusted OH rate constants. On the other hand,

801   CHCl₃ and 1,2-DCA mixing ratios, which are based on LBC rather than emissions in our model

802   – see Section 2.2 – are not sensitive to this 10% OH perturbation experiment. It shows that

803   further work is required to update the LBC values in the model or to develop global emission

804   inventories for CHCl₃ and 1,2-DCA.

805   For C₂Cl₄, the OH reaction is the major destruction pathway within the lower troposphere except

806   at high latitudes. As a result, the model NMB reduced by 5% in the OH perturbation experiment

807   (Figure S10). However, the role of Cl oxidation relative to OH is substantially larger than for

808   CH₂Cl₂ in the model. In the Arctic, there is a competition between OH and Cl oxidation

809   pathways while the Cl reaction prevails in the Antarctic region. In other latitude bins, the Cl

810   reaction is also found to be a dominant pathway in the free troposphere and UTLS region, in

811   good agreement with the model study of Hossaini et al. (2019) – see their Figure 2. The

812   photolysis reaction is not an important photochemical destruction pathway in the lower

813   troposphere for C₂Cl₄ either. However, photolysis of C₂Cl₄ becomes influential in the UTLS

814   region.
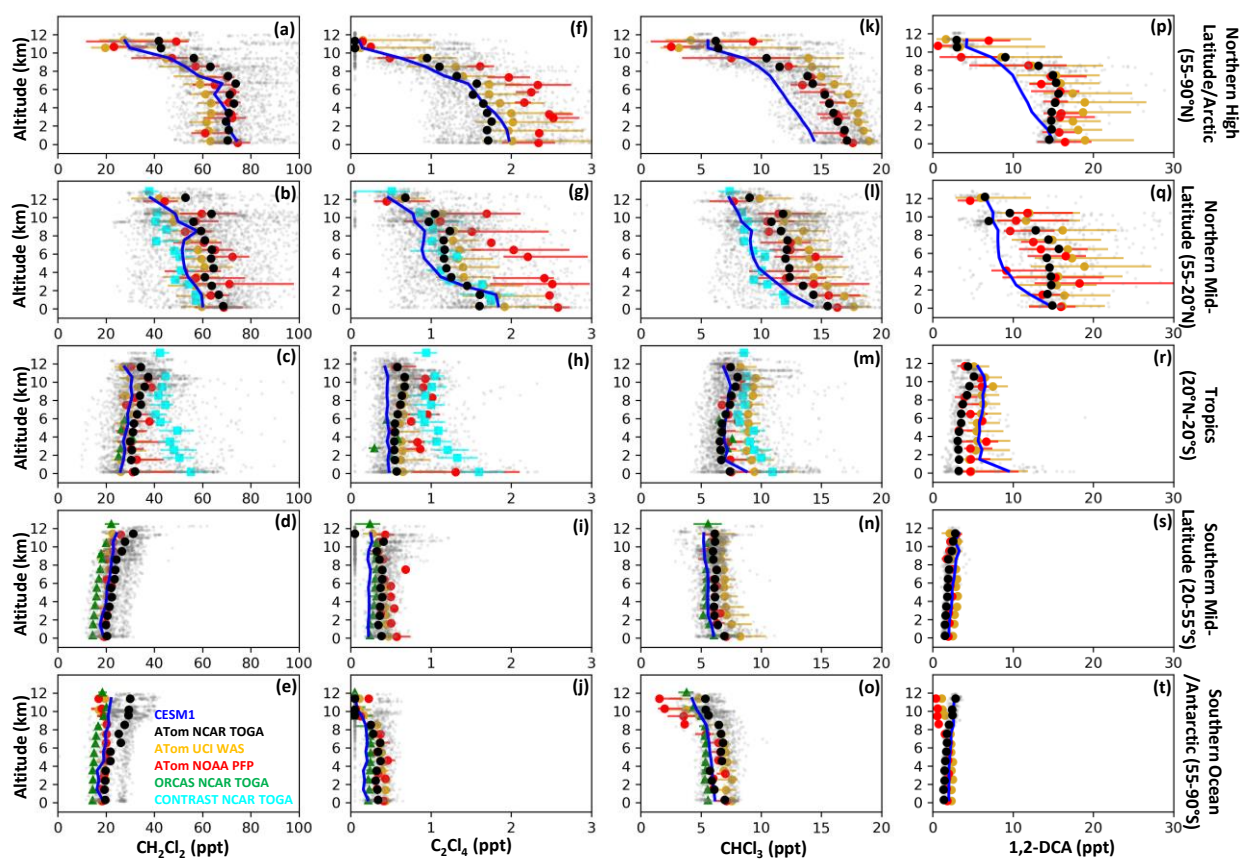
815

816   Figure **2** showed that modeled C_2Cl_4 was too low in the upper troposphere of the NH mid-latitude

817   region. Our k_{OH} perturbation experiment (Figure S10) shows an infinitesimal improvement for

818   C_2Cl_4, indicating the Cl reaction as its main destruction pathway. The Cl reaction being the

819   dominant pathway in high altitudes requires the presence of Cl atoms in the model. Inorganic

820   chlorine species are the main sources of Cl atoms in the troposphere (Wang et al., 2019b). Our

821   results suggest photolysis of molecular chlorine (Cl_2), formed due to acid displacement and

822   heterogeneous reactions (Li et al., 2022) including stoichiometric ice recycling in the UT

823   (Fernandez et al., 2014), as the potential source of Cl atoms in high latitudes in the model (Figure

824   S11). However, ATom measurements made by the NOAA chemical ionization mass

825   spectrometer (CIMS) instrument show a different spatial distribution (and mean abundance) of

826   Cl_2 with higher mixing ratios in the tropics and subtropical lower troposphere (Figure S12). Also,

827   the larger bias of modeled C_2Cl_4 in high altitudes over the mid-latitude region during the ATom

828   mission does not support the modeled dominant contribution through reactions with Cl atoms (
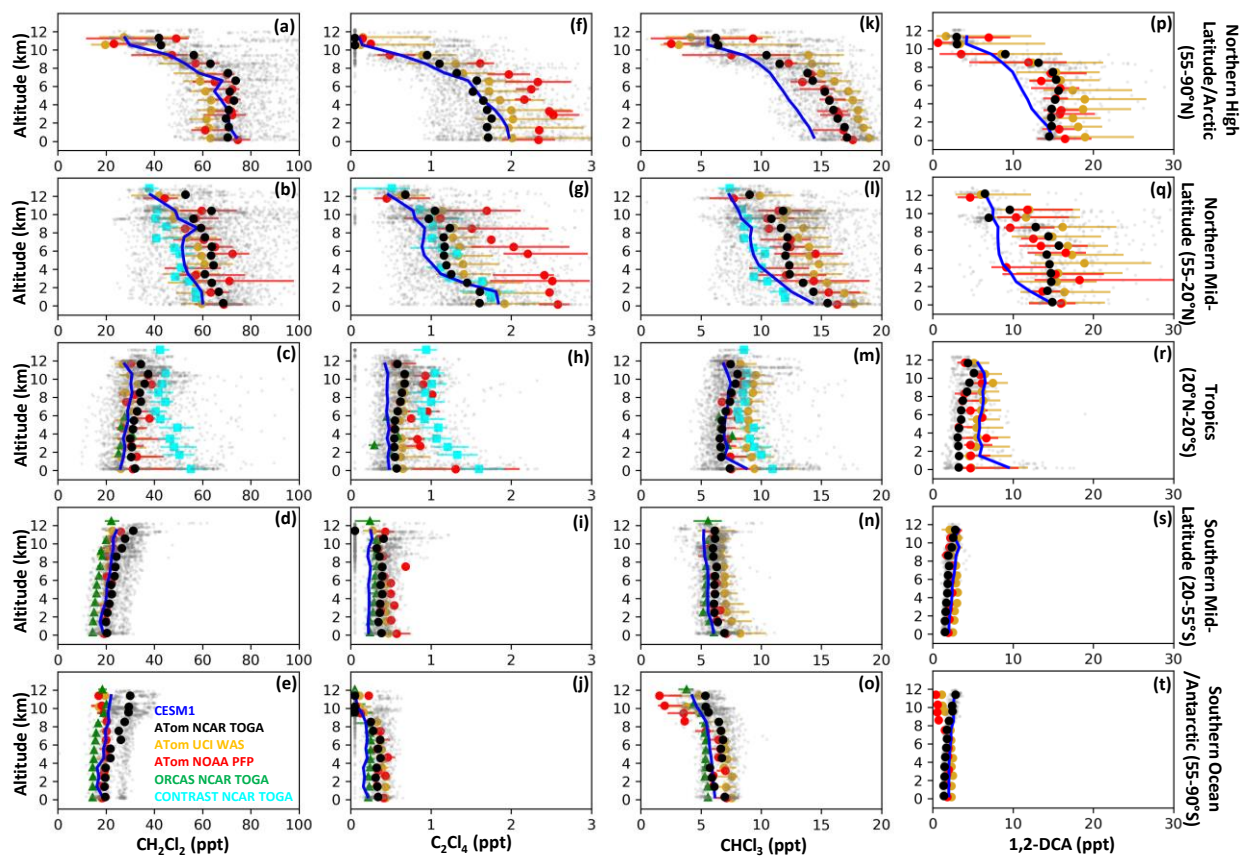
829

830   Figure 2). On the other hand, the source of active chlorine in the atmosphere has still large

831   uncertainties (Wang et al., 2021). Thus, we are investigating our model bias for Cl_2 but have not

832   resolved this.

833   Current emission estimates suggest that anthropogenic C_2Cl_4 emissions are about ten times lower

834   than CH_2Cl_2 (Claxton et al., 2020). However, the NH low-altitude (< 4 km or $\theta < 320$ K)

835   measured C_2Cl_4 to CH_2Cl_2 ratio is 0.02 during the ATom mission, which is consistent with the

836   shorter lifetime of C_2Cl_4 (Hossaini et al., 2019). Figure 12 shows the local lifetime of CH_2Cl_2

837   and C_2Cl_4 averaged between 2016 and 2018, calculated based on their partial destruction reaction

838   rates. Overall, the CH_2Cl_2 lifetime increases when moving from tropics towards the mid-latitudes

839   and higher altitudes, from ~75 days over the tropical boundary layer up to ~500 days around the

840   tropical tropopause. In addition, the CH_2Cl_2 local lifetime has a seasonal variation (Figure S13):

841   it is shorter in the NH during warmer seasons (e.g., JJA) than colder seasons (e.g., DJF).

842   Nevertheless, the shortest boundary layer CH_2Cl_2 local lifetime is always predicted to be over the

843   NH mid-latitudes (Figure S13).

844   The local lifetime of C_2Cl_4 is shorter than CH_2Cl_2, ranging between ~50 days in the tropical

845   boundary layer to ~100 days near the tropical tropopause. This is primarily due to the strong

846   oxidation rate of C_2Cl_4 with Cl atoms in our model as discussed above. Figure 12 also shows the

847   C_2Cl_4 local lifetime without considering the Cl destruction pathway, which resembles more to

848   the shape of CH_2Cl_2 local lifetime plots. Regardless, C_2Cl_4 without the Cl destruction pathway

849   still has a shorter lifetime than CH_2Cl_2 in the UTLS region. The shorter lifetime (and more

850   chlorine atoms per molecule) of C_2Cl_4 in the UTLS region suggests that in a case of deep

851   convection, on a molecule/molecule basis, C_2Cl_4 more rapidly liberates its Cl in the UTLS

852   compared to CH_2Cl_2.

853
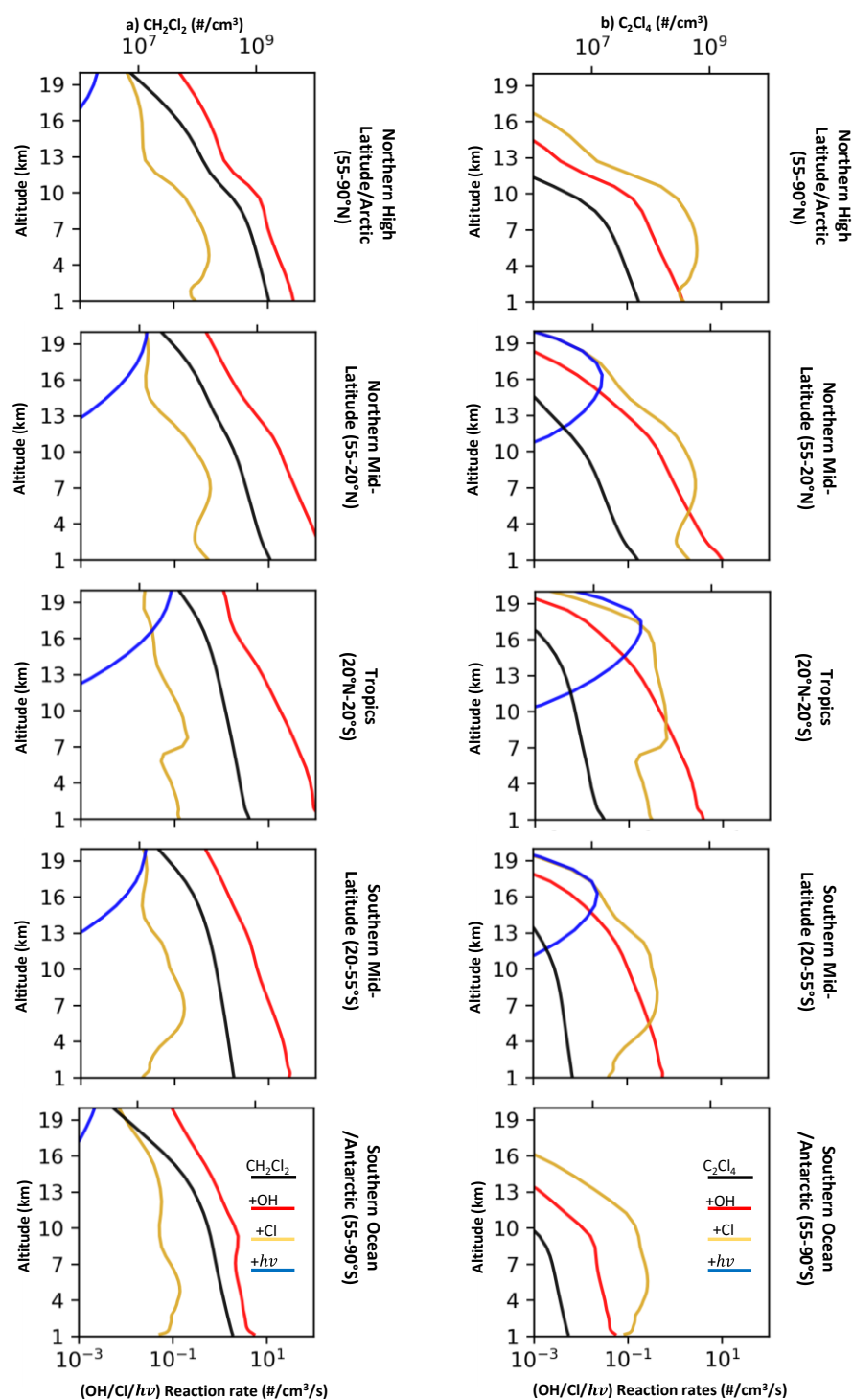
Figure 11. Vertical profiles of 2016–2018 annual mean modeled mixing ratios (black; top *x*-axis) and reaction rates
(colors; bottom *x*-axis) for CH$_2$Cl$_2$ (left column) and C$_2$Cl$_4$ (right column) over five latitude bins around the world
(not only along ATom flight tracks – see text). Note that *x*-axes are in logarithmic scale.
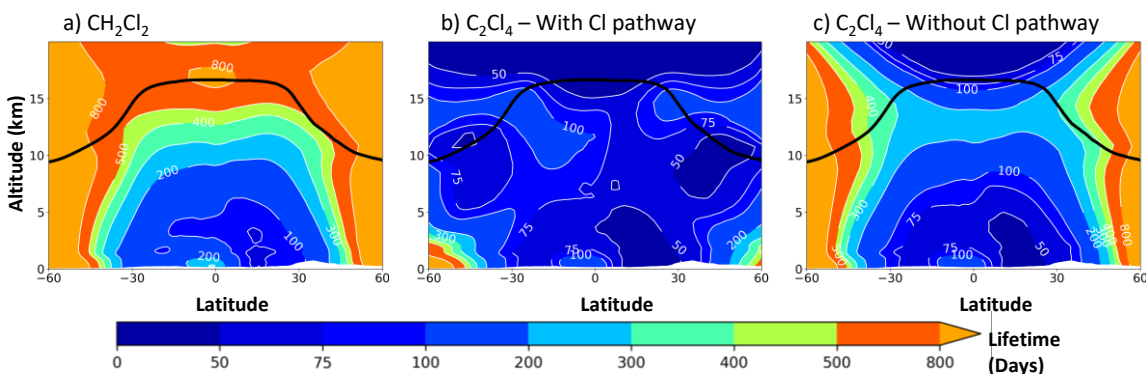
Figure 12. Modeled zonal 2016–2018 annual mean local lifetimes of (a) CH_2Cl_2 and (b-c) C_2Cl_4. Panel (b) shows the C_2Cl_4 local lifetime based on all the reactions (OH, Cl, and $h\nu$) while (c) includes only OH reaction and photolysis (i.e., without Cl pathway). The solid line shows the mean tropopause location.

4. Summary and conclusions

In this study, measurements of four Cl-VSLS from surface and aircraft-based programs are compared to the CESM model that includes updated chlorine chemistry. The bulk of the analyses focus on ATom data, which provided geographical coverage throughout the Pacific and Atlantic troposphere and nearly pole to pole. The detailed emission inventories for CH_2Cl_2 and C_2Cl_4 by Claxton et al. (2020) are used in the model. The $CHCl_3$ is prescribed as surface boundary condition (versus emissions) as it is largely emitted by natural sources, and its emissions are less well known although recent studies have tried to constrain its growing anthropogenic emissions (Fang et al., 2019; An et al., 2023). Similarly, 1,2-dichloroethane (1,2-DCA) is prescribed as surface boundary conditions as its emissions are even less well known than $CHCl_3$.

Aircraft-based measurement data from the NCAR TOGA, UCI WAS and NOAA PFP instruments are presented and compared. The agreement between the measurements is reasonably good and generally within reported uncertainties, but some significant differences exist, which have not yet been resolved. For example, a fairly large discrepancy (up to 60% = 17 ppt for CH_2Cl_2) in the high altitudes of the Southern Ocean and Antarctic region during ATom-3 and ATom-4.

The bulk of the model-measurement comparisons were made using the NCAR TOGA data for which there is the greatest spatial coverage. Detailed comparisons are presented for CH_2Cl_2 and C_2Cl_4. The model does a reasonable job of simulating the vertical profiles of all four Cl-VSLS species. However, the model generally underestimated the mixing ratios of CH_2Cl_2, most significantly in the northern mid-latitudes and tropics; it also generally underestimated C_2Cl_4,

46

882   particularly in the tropics and southern latitudes. The model comparisons with surface

883   observations from AGAGE and NOAA networks indicate a reasonable representation of the Cl-

884   VSLS mole fraction seasonal cycles in the model, with the global mean being biased low and

885   high for CH_2Cl_2 and C_2Cl_4, respectively. These biases primarily point to uncertainties in the

886   emissions, in terms of both magnitudes and global distribution.

887   Measurement profiles over the northern mid-latitudes show a large enhancement of CH_2Cl_2

888   mixing ratios over the Pacific Ocean compared to the Atlantic Ocean. We attribute this to the

889   Pacific being closer to the largest source region for this species and the lifetime of the species of

890   approximately four months, which precludes uniform hemispheric mixing. This is consistent

891   with our analysis of the regionally-tagged CH_2Cl_2 emissions. C_2Cl_4 and $CHCl_3$ also showed

892   general enhancements for the Pacific vs. Atlantic Ocean. In the NH, Cl-VSLS have sources that

893   are generally co-located and strong correlations between them were noted. The correlations

894   break down in the SH because $CHCl_3$ sources in the SH have a significant natural component

895   whereas CH_2Cl_2 and C_2Cl_4 do not (Worton et al., 2006; Feng et al., 2018). Significant NH/SH

896   gradients were observed for CH_2Cl_2 and C_2Cl_4 (and $CHCl_3$ and 1,2-DCA) owing to their source

897   locations and lifetimes with respect to interhemispheric mixing. This was a good test for the

898   model oxidation rates and transport capability and showed that the model simulated the inter-

899   hemispheric distribution of these Cl-VSLS quite well.

900   To further investigate how Cl-VSLS are redistributed globally after release from their sources,

901   we separated the globe into specific regions, and "tagged" model emissions for CH_2Cl_2 and

902   C_2Cl_4 from each of these regions and investigated their global distribution. The annual zonal

903   means of the tagged emissions showed that Asian emissions (AS) dominate the global

904   distributions of these species both near the surface (950 hPa) and at high altitudes (150 hPa),

905   representing up to 70% of the annual mean tropospheric mixing ratios of 36.9 ppt CH_2Cl_2 (73.8

906   ppt Cl). For C_2Cl_4, EU, NA, and AS are all important contributors to the global annual mean

907   modeled tropospheric mixing ratios of 0.73 ppt (2.92 ppt Cl). Therefore, the contribution of

908   source gas CH_2Cl_2 to the global Cl^{VSLS} burden is approximately 25 times larger than that arising

909   from C_2Cl_4 based on the modeling results averaged between 2016 and 2018. Similar calculations

910   using NCAR TOGA data, along the ATom flight tracks, led to a factor of $\approx$ 28 (using global

911   mean observed mixing ratios of 46.6 and 0.84 ppt for CH_2Cl_2 and C_2Cl_4, respectively).

912 Finally, we investigate the primary loss pathways for CH_2Cl_2 and C_2Cl_4 as a function of altitude

913 and latitude within the model framework and we find that reaction with OH dominates the loss

914 rate of CH_2Cl_2 at all latitudes and altitudes while photolysis plays only a minor role and only at

915 high altitudes. For C_2Cl_4, the reaction with OH represents the most significant loss process, but

916 given the Cl abundances calculated in the model, the reaction with chlorine atoms is competitive

917 with OH in the mid-troposphere and UTLS region, while photolysis is a significant loss process

918 in the LS. This conclusion hinges on the accuracy of the Cl calculated in the model, and further

919 analysis is required to determine if the Cl loss pathway is overestimated in the model given

920 ATom observations of high concentrations of Cl_2 in the remote troposphere and the new Cl atom

921 formation mechanism proposed by van Herpen et al. (2023).

922 In summary, the datasets reported here have provided the best global data coverage to date for

923 Cl-VSLS species and have provided us with the opportunity to test our understanding of global

924 distributions by comparing the measurements with model simulations. The model provided

925 insights into global distributions and pathways. Overall, the model did a reasonable job but

926 missed some observed features such as enhanced low-altitude concentrations of Cl-VSLS

927 (potentially due to both magnitudes and distribution of emissions) and Cl_2 concentrations in the

928 free troposphere that require further study. In our future work, we will study the impact of global

929 atmospheric circulation phenomena such as Asian Summer Monsoon Anticyclone and the North

930 American Monsoon Anticyclone as fast transport pathways of VSLS to the UTLS region, by

931 utilizing the data measured during the 2022 Asian Summer Monsoon Chemical and Climate

932 Impact Project (ACCLIP) and 2021–2022 Dynamics and Chemistry of the Summer Stratosphere

933 (DCOTSS) missions, respectively.

Data Availability

935 CAM-chem is a component of the NCAR CESM which is publicly available on the project

936 website (http://www.cesm.ucar.edu/). The NCAR TOGA, UCI WAS, NOAA PFP, NOAA

937 CIMS, and ATHOS chemical composition data, and NASA DC-8 positional and meteorological

938 measurements for the NASA ATom campaign are available from Wofsy et al. (2021). The

939 ORCAS and CONTRAST data are publicly available from Apel (2017) and Apel and Hornbrook

940 (2014), respectively. The NOAA ground-based measurements were supported in part by

941 NOAA's Atmospheric Chemistry, Carbon Cycle and Climate Program of its Climate Program

942 Office and are available from https://gml.noaa.gov/hats/data.html and

943 https://gml.noaa.gov/aftp/data/hats/solvents/. Data from the AGAGE monitoring network are

944 available from https://agage.mit.edu/data/. The model results used in this study are available

945 from Zenodo data repository (https://doi.org/10.5281/zenodo.10021453, Roozitalab et al., 2023)

Competing Interests

947 The authors declare that they have no conflict of interest.

Acknowledgements

References

967 Adcock, K. E., Fraser, P. J., Hall, B. D., Langenfelds, R. L., Lee, G., Montzka, S. A., Oram, D.
968 E., Röckmann, T., Stroh, F., Sturges, W. T., Vogel, B., and Laube, J. C.: Aircraft-Based
969 Observations of Ozone-Depleting Substances in the Upper Troposphere and Lower Stratosphere
970 in and Above the Asian Summer Monsoon, J. Geophys. Res. Atmos., 126, e2020JD033137,
971 https://doi.org/10.1029/2020JD033137, 2021.

972
973 An, M., Western, L. M., Say, D., Chen, L., Claxton, T., Ganesan, A. L., Hossaini, R., Krummel,
974 P. B., Manning, A. J., Mühle, J., O'Doherty, S., Prinn, R. G., Weiss, R. F., Young, D., Hu, J.,
975 Yao, B., and Rigby, M.: Rapid increase in dichloromethane emissions from China inferred
976 through atmospheric observations, Nat. Commun., 12, 7279, https://doi.org/10.1038/s41467-021-
977 27592-y, 2021.
978
979 An, M., Western, L. M., Hu, J., Yao, B., Mühle, J., Ganesan, A. L., Prinn, R. G., Krummel, P.
980 B., Hossaini, R., Fang, X., O'Doherty, S., Weiss, R. F., Young, D., and Rigby, M.:
981 Anthropogenic Chloroform Emissions from China Drive Changes in Global Emissions,
982 Environmental Science & Technology, 10.1021/acs.est.3c01898, 2023.
983
984 Andrews, S. J., Carpenter, L. J., Apel, E. C., Atlas, E., Donets, V., Hopkins, J. R., Hornbrook, R.
985 S., Lewis, A. C., Lidster, R. T., Lueb, R., Minaeian, J., Navarro, M., Punjabi, S., Riemer, D., and
986 Schauffler, S.: A comparison of very short lived halocarbon (VSLS) and DMS aircraft
987 measurements in the tropical west Pacific from CAST, ATTREX and CONTRAST, Atmos.
988 Meas. Tech., 9, 5213-5225, https://doi.org/10.5194/amt-9-5213-2016, 2016.
989
990 Apel, E. C., and Hornbrook, R. S.: NSF/NCAR GV HIAPER TOGA VOC Analyzer Data.
991 Version 1.0. , Journal, Volume, Pages, https://doi.org/10.5065/D6NG4P0F, 2014. access: 31
992 May 2023,
993
994 Apel, E. C., Hornbrook, R. S., Hills, A. J., Blake, N. J., Barth, M. C., Weinheimer, A., Cantrell,
995 C., Rutledge, S. A., Basarab, B., Crawford, J., Diskin, G., Homeyer, C. R., Campos, T., Flocke,
996 F., Fried, A., Blake, D. R., Brune, W., Pollack, I., Peischl, J., Ryerson, T., Wennberg, P. O.,
997 Crounse, J. D., Wisthaler, A., Mikoviny, T., Huey, G., Heikes, B., O'Sullivan, D., and Riemer,
998 D. D.: Upper tropospheric ozone production from lightning NOx-impacted convection: Smoke
999 ingestion case study from the DC3 campaign, J. Geophys. Res. Atmos., 120, 2505-2523,
1000 https://doi.org/10.1002/2014JD022121, 2015.
1001
1002 Apel, E. C.: ORCAS Trace Organic Gas Analyzer (TOGA) VOC Data Version 1.0., Journal,
1003 Volume, Pages, https://doi.org/10.5065/D6639N5B, 2017. access: 31 May 2023,
1004
1005 Butler, R., Palmer, P. I., Feng, L., Andrews, S. J., Atlas, E. L., Carpenter, L. J., Donets, V.,
1006 Harris, N. R. P., Montzka, S. A., Pan, L. L., Salawitch, R. J., and Schauffler, S. M.: Quantifying
1007 the vertical transport of CHBr3 and CH2Br2 over the western Pacific, Atmos. Chem. Phys., 18,
1008 13135-13153, 10.5194/acp-18-13135-2018, 2018.
1009
1010 Carpenter, L. J., and Liss, P. S.: On temperate sources of bromoform and other reactive organic
1011 bromine gases, J. Geophys. Res. Atmos., 105, 20539-20547,
1012 https://doi.org/10.1029/2000JD900242, 2000.
1013
1014 Chipperfield, M. P., Hossaini, R., Montzka, S. A., Reimann, S., Sherry, D., and Tegtmeier, S.:
1015 Renewed and emerging concerns over the production and emission of ozone-depleting
1016 substances, Nat. Rev. Earth Environ., 1, 251-263, 10.1038/s43017-020-0048-8, 2020.
1017

1018 Claxton, T., Hossaini, R., Wilson, C., Montzka, S. A., Chipperfield, M. P., Wild, O., Bednarz, E.
1019 M., Carpenter, L. J., Andrews, S. J., Hackenberg, S. C., Mühle, J., Oram, D., Park, S., Park, M.-
1020 K., Atlas, E., Navarro, M., Schauffler, S., Sherry, D., Vollmer, M., Schuck, T., Engel, A.,
1021 Krummel, P. B., Maione, M., Arduini, J., Saito, T., Yokouchi, Y., O'Doherty, S., Young, D., and
1022 Lunder, C.: A Synthesis Inversion to Constrain Global Emissions of Two Very Short Lived
1023 Chlorocarbons: Dichloromethane, and Perchloroethylene, J. Geophys. Res. Atmos., 125,
1024 e2019JD031818, https://doi.org/10.1029/2019JD031818, 2020.

1026 Daniel, J. S., Solomon, S., Portmann, R. W., and Garcia, R. R.: Stratospheric ozone destruction:
1027 The importance of bromine relative to chlorine, Journal of Geophysical Research: Atmospheres,
1028 104, 23871-23880, https://doi.org/10.1029/1999JD900381, 1999.

1030 Deming, B. L., Pagonis, D., Liu, X., Day, D. A., Talukdar, R., Krechmer, J. E., de Gouw, J. A.,
1031 Jimenez, J. L., and Ziemann, P. J.: Measurements of delays of gas-phase compounds in a wide
1032 variety of tubing materials due to gas–wall interactions, Atmos. Meas. Tech., 12, 3453-3461,
1033 10.5194/amt-12-3453-2019, 2019.

1035 Dhomse, S. S., Feng, W., Montzka, S. A., Hossaini, R., Keeble, J., Pyle, J. A., Daniel, J. S., and
1036 Chipperfield, M. P.: Delay in recovery of the Antarctic ozone hole from unexpected CFC-11
1037 emissions, Nat. Commun., 10, 5781, 10.1038/s41467-019-13717-x, 2019.

1039 Emmons, L. K., Walters, S., Hess, P. G., Lamarque, J. F., Pfister, G. G., Fillmore, D., Granier,
1040 C., Guenther, A., Kinnison, D., Laepple, T., Orlando, J., Tie, X., Tyndall, G., Wiedinmyer, C.,
1041 Baughcum, S. L., and Kloster, S.: Description and evaluation of the Model for Ozone and
1042 Related chemical Tracers, version 4 (MOZART-4), Geosci. Model Dev., 3, 43-67,
1043 https://doi.org/10.5194/gmd-3-43-2010, 2010.

1045 Emmons, L. K., Hess, P. G., Lamarque, J. F., and Pfister, G. G.: Tagged ozone mechanism for
1046 MOZART-4, CAM-chem and other chemical transport models, Geosci. Model Dev., 5, 1531-
1047 1542, https://doi.org/10.5194/gmd-5-1531-2012, 2012.

1049 Engel, A., Rigby, M., Burkholder, J. B., Fernandez, R. P., Froidevaux, L., Hall, B. D., Hossaini,
1050 R., Saito, T., Vollmer, M. K., and Yao, B.: Update on ozone-depleting substances (ODSs) and
1051 other gases of interest to the Montreal Protocol, Chapter 1 in Scientific Assessment of Ozone
1052 Depletion, Global Ozone Research and Monitoring Project - Report No. 58, 2018.

1054 Fang, X., Park, S., Saito, T., Tunnicliffe, R., Ganesan, A. L., Rigby, M., Li, S., Yokouchi, Y.,
1055 Fraser, P. J., Harth, C. M., Krummel, P. B., Mühle, J., O'Doherty, S., Salameh, P. K., Simmonds,
1056 P. G., Weiss, R. F., Young, D., Lunt, M. F., Manning, A. J., Gressent, A., and Prinn, R. G.:
1057 Rapid increase in ozone-depleting chloroform emissions from China, Nat. Geosci., 12, 89-93,
1058 https://doi.org/10.1038/s41561-018-0278-2, 2019.

1060 Feng, Y., Bie, P., Wang, Z., Wang, L., and Zhang, J.: Bottom-up anthropogenic dichloromethane
1061 emission estimates from China for the period 2005–2016 and predictions of future emissions,
1062 Atmos. Environ., 186, 241-247, https://doi.org/10.1016/j.atmosenv.2018.05.039, 2018.
1063

1064   Fernandez, R. P., Salawitch, R. J., Kinnison, D. E., Lamarque, J. F., and Saiz-Lopez, A.:
1065   Bromine partitioning in the tropical tropopause layer: implications for stratospheric injection,
1066   Atmos. Chem. Phys., 14, 13391-13410, https://doi.org/10.5194/acp-14-13391-2014, 2014.
1067
1068   Gelaro, R., McCarty, W., Suárez, M. J., Todling, R., Molod, A., Takacs, L., Randles, C. A.,
1069   Darmenov, A., Bosilovich, M. G., Reichle, R., Wargan, K., Coy, L., Cullather, R., Draper, C.,
1070   Akella, S., Buchard, V., Conaty, A., da Silva, A. M., Gu, W., Kim, G.-K., Koster, R., Lucchesi,
1071   R., Merkova, D., Nielsen, J. E., Partyka, G., Pawson, S., Putman, W., Rienecker, M., Schubert,
1072   S. D., Sienkiewicz, M., and Zhao, B.: The Modern-Era Retrospective Analysis for Research and
1073   Applications, Version 2 (MERRA-2), J. Clim., 30, 5419-5454, https://doi.org/10.1175/JCLI-D-
1074   16-0758.1, 2017.
1075
1076   Granier, C., Darras, S., van Der Gon, H. D., Jana, D., Elguindi, N., Bo, G., Michael, G., Marc,
1077   G., Jalkanen, J.-P., and Kuenen, J.: The Copernicus atmosphere monitoring service global and
1078   regional emissions (April 2019 version), 2019.
1079
1080   Guenther, A. B., Jiang, X., Heald, C. L., Sakulyanontvittaya, T., Duhl, T., Emmons, L. K., and
1081   Wang, X.: The Model of Emissions of Gases and Aerosols from Nature version 2.1
1082   (MEGAN2.1): an extended and updated framework for modeling biogenic emissions, Geosci.
1083   Model Dev., 5, 1471-1492, https://doi.org/10.5194/gmd-5-1471-2012, 2012.
1084
1085   Harris, N. R. P., Carpenter, L. J., Lee, J. D., Vaughan, G., Filus, M. T., Jones, R. L., OuYang, B.,
1086   Pyle, J. A., Robinson, A. D., Andrews, S. J., Lewis, A. C., Minaeian, J., Vaughan, A., Dorsey, J.
1087   R., Gallagher, M. W., Le Breton, M., Newton, R., Percival, C. J., Ricketts, H. M. A., Bauguitte,
1088   S. J. B., Nott, G. J., Wellpott, A., Ashfold, M. J., Flemming, J., Butler, R., Palmer, P. I., Kaye, P.
1089   H., Stopford, C., Chemel, C., Boesch, H., Humpage, N., Vick, A., MacKenzie, A. R., Hyde, R.,
1090   Angelov, P., Meneguz, E., and Manning, A. J.: Coordinated Airborne Studies in the Tropics
1091   (CAST), Bull. Am. Meteorol., 98, 145-162, https://doi.org/10.1175/BAMS-D-14-00290.1, 2017.
1092
1093   Hoesly, R. M., Smith, S. J., Feng, L., Klimont, Z., Janssens-Maenhout, G., Pitkanen, T., Seibert,
1094   J. J., Vu, L., Andres, R. J., Bolt, R. M., Bond, T. C., Dawidowski, L., Kholod, N., Kurokawa, J.
1095   I., Li, M., Liu, L., Lu, Z., Moura, M. C. P., O'Rourke, P. R., and Zhang, Q.: Historical (1750–
1096   2014) anthropogenic emissions of reactive gases and aerosols from the Community Emissions
1097   Data System (CEDS), Geosci. Model Dev., 11, 369-408, https://doi.org/10.5194/gmd-11-369-
1098   2018, 2018.
1099
1100   Honomichl, S. B., and Pan, L. L.: Transport From the Asian Summer Monsoon Anticyclone
1101   Over the Western Pacific, J. Geophys. Res. Atmos., 125, e2019JD032094,
1102   https://doi.org/10.1029/2019JD032094, 2020.
1103
1104   Hossaini, R., Chipperfield, M. P., Saiz-Lopez, A., Fernandez, R., Monks, S., Feng, W., Brauer,
1105   P., and von Glasow, R.: A global model of tropospheric chlorine chemistry: Organic versus
1106   inorganic sources and impact on methane oxidation, J. Geophys. Res. Atmos., 121, 14,271-
1107   214,297, https://doi.org/10.1002/2016JD025756, 2016.
1108

1109 Hossaini, R., Chipperfield, M. P., Montzka, S. A., Leeson, A. A., Dhomse, S. S., and Pyle, J. A.:
1110 The increasing threat to stratospheric ozone from dichloromethane, Nat. Commun., 8, 15962,
1111 https://doi.org/10.1038/ncomms15962, 2017.
1112
1113 Hossaini, R., Atlas, E., Dhomse, S. S., Chipperfield, M. P., Bernath, P. F., Fernando, A. M.,
1114 Mühle, J., Leeson, A. A., Montzka, S. A., Feng, W., Harrison, J. J., Krummel, P., Vollmer, M.
1115 K., Reimann, S., O'Doherty, S., Young, D., Maione, M., Arduini, J., and Lunder, C. R.: Recent
1116 Trends in Stratospheric Chlorine From Very Short-Lived Substances, J. Geophys. Res. Atmos.,
1117 124, 2318-2335, https://doi.org/10.1029/2018JD029400, 2019.
1118
1119 Hu, L., Montzka, S. A., Miller, J. B., Andrews, A. E., Lehman, S. J., Miller, B. R., Thoning, K.,
1120 Sweeney, C., Chen, H., Godwin, D. S., Masarie, K., Bruhwiler, L., Fischer, M. L., Biraud, S. C.,
1121 Torn, M. S., Mountain, M., Nehrkorn, T., Eluszkiewicz, J., Miller, S., Draxler, R. R., Stein, A.
1122 F., Hall, B. D., Elkins, J. W., and Tans, P. P.: U.S. emissions of HFC-134a derived for 2008–
1123 2012 from an extensive flask-air sampling network, J. Geophys. Res. Atmos., 120, 801-825,
1124 https://doi.org/10.1002/2014JD022617, 2015.
1125
1126 Hurrell, J. W., Holland, M. M., Gent, P. R., Ghan, S., Kay, J. E., Kushner, P. J., Lamarque, J. F.,
1127 Large, W. G., Lawrence, D., Lindsay, K., Lipscomb, W. H., Long, M. C., Mahowald, N., Marsh,
1128 D. R., Neale, R. B., Rasch, P., Vavrus, S., Vertenstein, M., Bader, D., Collins, W. D., Hack, J. J.,
1129 Kiehl, J., and Marshall, S.: The Community Earth System Model: A Framework for
1130 Collaborative Research, Bull. Am. Meteorol., 94, 1339-1360, https://doi.org/10.1175/BAMS-D-
1131 12-00121.1, 2013.
1132
1133 Jesswein, M., Fernandez, R. P., Berná, L., Saiz-Lopez, A., Grooß, J. U., Hossaini, R., Apel, E.
1134 C., Hornbrook, R. S., Atlas, E. L., Blake, D. R., Montzka, S., Keber, T., Schuck, T.,
1135 Wagenhäuser, T., and Engel, A.: Global seasonal distribution of CH2Br2 and CHBr3 in the
1136 upper troposphere and lower stratosphere, Atmos. Chem. Phys., 22, 15049-15070,
1137 https://doi.org/10.5194/acp-22-15049-2022, 2022.
1138
1139 Keber, T., Bönisch, H., Hartick, C., Hauck, M., Lefrancois, F., Obersteiner, F., Ringsdorf, A.,
1140 Schohl, N., Schuck, T., Hossaini, R., Graf, P., Jöckel, P., and Engel, A.: Bromine from short-
1141 lived source gases in the extratropical northern hemispheric upper troposphere and lower
1142 stratosphere (UTLS), Atmos. Chem. Phys., 20, 4105-4132, https://doi.org/10.5194/acp-20-4105-
1143 2020, 2020.
1144
1145 Keene, W. C., Khalil, M. A. K., Erickson Iii, D. J., McCulloch, A., Graedel, T. E., Lobert, J. M.,
1146 Aucott, M. L., Gong, S. L., Harper, D. B., Kleiman, G., Midgley, P., Moore, R. M., Seuzaret, C.,
1147 Sturges, W. T., Benkovitz, C. M., Koropalov, V., Barrie, L. A., and Li, Y. F.: Composite global
1148 emissions of reactive chlorine from anthropogenic and natural sources: Reactive Chlorine
1149 Emissions Inventory, J. Geophys. Res. Atmos., 104, 8429-8440,
1150 https://doi.org/10.1029/1998JD100084, 1999.
1151
1152 Keng, F. S.-L., Phang, S.-M., Abd Rahman, N., Yeong, H.-Y., Malin, G., Leedham Elvidge, E.,
1153 and Sturges, W.: Halocarbon emissions by selected tropical seaweeds exposed to different

1154 temperatures, Phytochem., 190, 112869, https://doi.org/10.1016/j.phytochem.2021.112869,
1155 2021.
1156
1157 Khalil, M.A.K., Rasmussen, R.A.,: Atmospheric chloroform. Atmos. Environ. 33, 7, 1151–1158,
1158 https://doi.org/10.1016/S1352-2310(98)00233-7, 1999.
1159
1160 Kinnison, D. E., Brasseur, G. P., Walters, S., Garcia, R. R., Marsh, D. R., Sassi, F., Harvey, V.
1161 L., Randall, C. E., Emmons, L., Lamarque, J. F., Hess, P., Orlando, J. J., Tie, X. X., Randel, W.,
1162 Pan, L. L., Gettelman, A., Granier, C., Diehl, T., Niemeier, U., and Simmons, A. J.: Sensitivity
1163 of chemical tracers to meteorological parameters in the MOZART-3 chemical transport model, J.
1164 Geophys. Res. Atmos., 112, https://doi.org/10.1029/2006JD007879, 2007.
1165
1166 Klobas, J. E., Weisenstein, D. K., Salawitch, R. J., and Wilmouth, D. M.: Reformulating the
1167 bromine alpha factor and equivalent effective stratospheric chlorine (EESC): evolution of ozone
1168 destruction rates of bromine and chlorine in future climate scenarios, Atmos. Chem. Phys., 20,
1169 9459-9471, https://doi.org/10.5194/acp-20-9459-2020, 2020.
1170
1171 Lamarque, J. F., Emmons, L. K., Hess, P. G., Kinnison, D. E., Tilmes, S., Vitt, F., Heald, C. L.,
1172 Holland, E. A., Lauritzen, P. H., Neu, J., Orlando, J. J., Rasch, P. J., and Tyndall, G. K.: CAM-
1173 chem: description and evaluation of interactive atmospheric chemistry in the Community Earth
1174 System Model, Geosci. Model Dev., 5, 369-411, https://doi.org/10.5194/gmd-5-369-2012, 2012.
1175
1176 Laturnus, F., Haselmann, K. F., Borch, T., and Grøn, C.: Terrestrial natural sources of
1177 trichloromethane (chloroform, CHCl3) – An overview, Biogeochemistry, 60, 121-139,
1178 10.1023/A:1019887505651, 2002.
1179
1180 Laube, J. C., Tegtmeier, S., Fernandez, R. P., Harrison, J. J., Hu, L., Krummel, P. B., Mahieu, E.,
1181 Park, S., and Western, L. M.: Update on ozone-depleting substances (ODSs) and other gases of
1182 interest to the Montreal Protocol, Chapter 1 in Scientific Assessment of Ozone Depletion, Global
1183 Ozone Research and Monitoring Project - Report No. 278, 2022.
1184
1185 Lauther, V., Vogel, B., Wintel, J., Rau, A., Hoor, P., Bense, V., Müller, R., and Volk, C. M.: In
1186 situ observations of CH2Cl2 and CHCl3 show efficient transport pathways for very short-lived
1187 species into the lower stratosphere via the Asian and the North American summer monsoon,
1188 Atmos. Chem. Phys., 22, 2049-2077, https://doi.org/10.5194/acp-22-2049-2022, 2022.
1189
1190 Leedham Elvidge, E. C., Oram, D. E., Laube, J. C., Baker, A. K., Montzka, S. A., Humphrey, S.,
1191 O'Sullivan, D. A., and Brenninkmeijer, C. A. M.: Increasing concentrations of dichloromethane,
1192 CH2Cl2, inferred from CARIBIC air samples collected 1998–2012, Atmos. Chem. Phys., 15,
1193 1939-1958, https://doi.org/10.5194/acp-15-1939-2015, 2015.
1194
1195 Li, Q., Fernandez, R. P., Hossaini, R., Iglesias-Suarez, F., Cuevas, C. A., Apel, E. C., Kinnison,
1196 D. E., Lamarque, J.-F., and Saiz-Lopez, A.: Reactive halogens increase the global methane
1197 lifetime and radiative forcing in the 21st century, Nat. Commun., 13, 2768,
1198 https://doi.org/10.1038/s41467-022-30456-8, 2022.
1199

1200   Neale, R., Richter, J., Park, S., Lauritzen, P., Vavrus, S., Rasch, P., and Zhang, M.: The mean
1201   climate of the Community Atmosphere Model (CAM4) in forced SST and fully coupled
1202   experiments, J. Clim., 26, 5150-5168, https://doi.org/10.1175/JCLI-D-12-00236.1, 2013.
1203
1204   Nicely, J. M., Duncan, B. N., Hanisco, T. F., Wolfe, G. M., Salawitch, R. J., Deushi, M.,
1205   Haslerud, A. S., Jöckel, P., Josse, B., Kinnison, D. E., Klekociuk, A., Manyin, M. E., Marécal,
1206   V., Morgenstern, O., Murray, L. T., Myhre, G., Oman, L. D., Pitari, G., Pozzer, A., Quaglia, I.,
1207   Revell, L. E., Rozanov, E., Stenke, A., Stone, K., Strahan, S., Tilmes, S., Tost, H., Westervelt, D.
1208   M., and Zeng, G.: A machine learning examination of hydroxyl radical differences among model
1209   simulations for CCMI-1, Atmos. Chem. Phys., 20, 1341-1361, 10.5194/acp-20-1341-2020, 2020.
1210
1211   Oelhaf, H., Sinnhuber, B.-M., Woiwode, W., Bönisch, H., Bozem, H., Engel, A., Fix, A., Friedl-
1212   Vallon, F., Grooß, J.-U., Hoor, P., Johansson, S., Jurkat-Witschas, T., Kaufmann, S., Krämer,
1213   M., Krause, J., Kretschmer, E., Lörks, D., Marsing, A., Orphal, J., Pfeilsticker, K., Pitts, M.,
1214   Poole, L., Preusse, P., Rapp, M., Riese, M., Rolf, C., Ungermann, J., Voigt, C., Volk, C. M.,
1215   Wirth, M., Zahn, A., and Ziereis, H.: POLSTRACC: Airborne Experiment for Studying the Polar
1216   Stratosphere in a Changing Climate with the High Altitude and Long Range Research Aircraft
1217   (HALO), Bull. Am. Meteorol., 100, 2634-2664, https://doi.org/10.1175/BAMS-D-18-0181.1,
1218   2019.
1219
1220   Oram, D. E., Ashfold, M. J., Laube, J. C., Gooch, L. J., Humphrey, S., Sturges, W. T., Leedham-
1221   Elvidge, E., Forster, G. L., Harris, N. R. P., Mead, M. I., Samah, A. A., Phang, S. M., Ou-Yang,
1222   C. F., Lin, N. H., Wang, J. L., Baker, A. K., Brenninkmeijer, C. A. M., and Sherry, D.: A
1223   growing threat to the ozone layer from short-lived anthropogenic chlorocarbons, Atmos. Chem.
1224   Phys., 17, 11929-11941, https://doi.org/10.5194/acp-17-11929-2017, 2017.
1225
1226   Ordóñez, C., Lamarque, J. F., Tilmes, S., Kinnison, D. E., Atlas, E. L., Blake, D. R., Sousa
1227   Santos, G., Brasseur, G., and Saiz-Lopez, A.: Bromine and iodine chemistry in a global
1228   chemistry-climate model: description and evaluation of very short-lived oceanic sources, Atmos.
1229   Chem. Phys., 12, 1423-1447, https://doi.org/10.5194/acp-12-1423-2012, 2012.
1230
1231   Pan, L. L., Atlas, E. L., Salawitch, R. J., Honomichl, S. B., Bresch, J. F., Randel, W. J., Apel, E.
1232   C., Hornbrook, R. S., Weinheimer, A. J., Anderson, D. C., Andrews, S. J., Baidar, S., Beaton, S.
1233   P., Campos, T. L., Carpenter, L. J., Chen, D., Dix, B., Donets, V., Hall, S. R., Hanisco, T. F.,
1234   Homeyer, C. R., Huey, L. G., Jensen, J. B., Kaser, L., Kinnison, D. E., Koenig, T. K., Lamarque,
1235   J. F., Liu, C., Luo, J., Luo, Z. J., Montzka, D. D., Nicely, J. M., Pierce, R. B., Riemer, D. D.,
1236   Robinson, T., Romashkin, P., Saiz-Lopez, A., Schauffler, S., Shieh, O., Stell, M. H., Ullmann,
1237   K., Vaughan, G., Volkamer, R., and Wolfe, G.: The Convective Transport of Active Species in
1238   the Tropics (CONTRAST) Experiment, Bull. Am. Meteorol., 98, 106-128,
1239   https://doi.org/10.1175/BAMS-D-14-00272.1, 2017.
1240
1241   Prather, M. J., Holmes, C. D., and Hsu, J.: Reactive greenhouse gas scenarios: Systematic
1242   exploration of uncertainties and the role of atmospheric chemistry, Geophysical Research
1243   Letters, 39, https://doi.org/10.1029/2012GL051440, 2012.
1244

1245 Prinn, R. G., Weiss, R. F., Fraser, P. J., Simmonds, P. G., Cunnold, D. M., Alyea, F. N.,
1246 O'Doherty, S., Salameh, P., Miller, B. R., Huang, J., Wang, R. H. J., Hartley, D. E., Harth, C.,
1247 Steele, L. P., Sturrock, G., Midgley, P. M., and McCulloch, A.: A history of chemically and
1248 radiatively important gases in air deduced from ALE/GAGE/AGAGE, J. Geophys. Res. Atmos.,
1249 105, 17751-17792, https://doi.org/10.1029/2000JD900141, 2000.

1251 Prinn, R. G., Weiss, R. F., Arduini, J., Arnold, T., DeWitt, H. L., Fraser, P. J., Ganesan, A. L.,
1252 Gasore, J., Harth, C. M., Hermansen, O., Kim, J., Krummel, P. B., Li, S., Loh, Z. M., Lunder, C.
1253 R., Maione, M., Manning, A. J., Miller, B. R., Mitrevski, B., Mühle, J., O'Doherty, S., Park, S.,
1254 Reimann, S., Rigby, M., Saito, T., Salameh, P. K., Schmidt, R., Simmonds, P. G., Steele, L. P.,
1255 Vollmer, M. K., Wang, R. H., Yao, B., Yokouchi, Y., Young, D., and Zhou, L.: History of
1256 chemically and radiatively important atmospheric gases from the Advanced Global Atmospheric
1257 Gases Experiment (AGAGE), Earth Syst. Sci. Data, 10, 985-1018, https://doi.org/10.5194/essd-
1258 10-985-2018, 2018.

1260 Roozitalab, B., Emmons, L. K., Hornbrook, R. S., Kinnison, D. E., Fernandez, R. P., Li, Q.,
1261 Saiz-Lopez, A., Hossaini, R., Cuevas, C. A., Hills, A. J., Montzka, S. A., Blake, D. R., Brune,
1262 W. H., Veres, P. R., Apel, E. C.: CESM Short lived Halogen simulation results for Roozitalab et
1263 al. (2023) in JGR-Atmospheres, Zenodo [data set], https://doi.org/ 10.5281/zenodo.10021453,
1264 2023.

1266 Saiz-Lopez, A., and von Glasow, R.: Reactive halogen chemistry in the troposphere, Chem. Soc.
1267 Rev., 41, 6448-6472, https://doi.org/10.1039/C2CS35208G, 2012.

1269 Saiz-Lopez, A., Fernandez, R. P., Ordóñez, C., Kinnison, D. E., Gómez Martín, J. C., Lamarque,
1270 J. F., and Tilmes, S.: Iodine chemistry in the troposphere and its effect on ozone, Atmos. Chem.
1271 Phys., 14, 13119-13143, 10.5194/acp-14-13119-2014, 2014.

1273 Say, D., Ganesan, A. L., Lunt, M. F., Rigby, M., O'Doherty, S., Harth, C., Manning, A. J.,
1274 Krummel, P. B., and Bauguitte, S.: Emissions of halocarbons from India inferred through
1275 atmospheric measurements, Atmos. Chem. Phys., 19, 9865-9885, https://doi.org/10.5194/acp-19-
1276 9865-2019, 2019.

1278 Simmonds, P. G., Manning, A. J., Cunnold, D. M., McCulloch, A., O'Doherty, S., Derwent, R.
1279 G., Krummel, P. B., Fraser, P. J., Dunse, B., Porter, L. W., Wang, R. H. J., Greally, B. R., Miller,
1280 B. R., Salameh, P., Weiss, R. F., and Prinn, R. G.: Global trends, seasonal cycles, and European
1281 emissions of dichloromethane, trichloroethene, and tetrachloroethene from the AGAGE
1282 observations at Mace Head, Ireland, and Cape Grim, Tasmania, J. Geophys. Res. Atmos., 111,
1283 https://doi.org/10.1029/2006JD007082, 2006.

1285 Simpson, I. J., Meinardi, S., Blake, N. J., Rowland, F. S., and Blake, D. R.: Long-term decrease
1286 in the global atmospheric burden of tetrachloroethene (C2Cl4), Geophys. Res. Lett., 31,
1287 https://doi.org/10.1029/2003GL019351, 2004.

1289 Simpson, I. J., Blake, N. J., Barletta, B., Diskin, G. S., Fuelberg, H. E., Gorham, K., Huey, L. G.,
1290 Meinardi, S., Rowland, F. S., Vay, S. A., Weinheimer, A. J., Yang, M., and Blake, D. R.:

1291 Characterization of trace gases measured over Alberta oil sands mining operations: 76 speciated
1292 C2–C10 volatile organic compounds (VOCs), CO2, CH4, CO, NO, NO2, NOy, O3 and SO2,
1293 Atmos. Chem. Phys., 10, 11931-11954, https://doi.org/10.5194/acp-10-11931-2010, 2010.
1294
1295 Simpson, W. R., Brown, S. S., Saiz-Lopez, A., Thornton, J. A., and von Glasow, R.:
1296 Tropospheric Halogen Chemistry: Sources, Cycling, and Impacts, Chem. Rev., 115, 4035-4062,
1297 https://doi.org/10.1021/cr5006638, 2015.
1298
1299 Sinnhuber, B. M., Sheode, N., Sinnhuber, M., Chipperfield, M. P., and Feng, W.: The
1300 contribution of anthropogenic bromine emissions to past stratospheric ozone trends: a modelling
1301 study, Atmos. Chem. Phys., 9, 2863-2871, 10.5194/acp-9-2863-2009, 2009.
1302
1303 Stephens, B. B., Long, M. C., Keeling, R. F., Kort, E. A., Sweeney, C., Apel, E. C., Atlas, E. L.,
1304 Beaton, S., Bent, J. D., Blake, N. J., Bresch, J. F., Casey, J., Daube, B. C., Diao, M., Diaz, E.,
1305 Dierssen, H., Donets, V., Gao, B.-C., Gierach, M., Green, R., Haag, J., Hayman, M., Hills, A. J.,
1306 Hoecker-Martínez, M. S., Honomichl, S. B., Hornbrook, R. S., Jensen, J. B., Li, R.-R.,
1307 McCubbin, I., McKain, K., Morgan, E. J., Nolte, S., Powers, J. G., Rainwater, B., Randolph, K.,
1308 Reeves, M., Schauffler, S. M., Smith, K., Smith, M., Stith, J., Stossmeister, G., Toohey, D. W.,
1309 and Watt, A. S.: The O2/N2 Ratio and CO2 Airborne Southern Ocean Study, Bull. Am.
1310 Meteorol., 99, 381-402, https://doi.org/10.1175/BAMS-D-16-0206.1, 2018.
1311
1312 Stevenson, D. S., Zhao, A., Naik, V., O'Connor, F. M., Tilmes, S., Zeng, G., Murray, L. T.,
1313 Collins, W. J., Griffiths, P. T., Shim, S., Horowitz, L. W., Sentman, L. T., and Emmons, L.:
1314 Trends in global tropospheric hydroxyl radical and methane lifetime since 1850 from
1315 AerChemMIP, Atmos. Chem. Phys., 20, 12905-12920, https://doi.org/10.5194/acp-20-12905-
1316 2020, 2020.
1317
1318 Sweeney, C., Karion, A., Wolter, S., Newberger, T., Guenther, D., Higgs, J. A., Andrews, A. E.,
1319 Lang, P. M., Neff, D., Dlugokencky, E., Miller, J. B., Montzka, S. A., Miller, B. R., Masarie, K.
1320 A., Biraud, S. C., Novelli, P. C., Crotwell, M., Crotwell, A. M., Thoning, K., and Tans, P. P.:
1321 Seasonal climatology of CO2 across North America from aircraft measurements in the
1322 NOAA/ESRL Global Greenhouse Gas Reference Network, J. Geophys. Res. Atmos., 120, 5155-
1323 5190, https://doi.org/10.1002/2014JD022591, 2015.
1324
1325 Thompson, C. R., Wofsy, S. C., Prather, M. J., Newman, P. A., Hanisco, T. F., Ryerson, T. B.,
1326 Fahey, D. W., Apel, E. C., Brock, C. A., Brune, W. H., Froyd, K., Katich, J. M., Nicely, J. M.,
1327 Peischl, J., Ray, E., Veres, P. R., Wang, S., Allen, H. M., Asher, E., Bian, H., Blake, D.,
1328 Bourgeois, I., Budney, J., Bui, T. P., Butler, A., Campuzano-Jost, P., Chang, C., Chin, M.,
1329 Commane, R., Correa, G., Crounse, J. D., Daube, B., Dibb, J. E., DiGangi, J. P., Diskin, G. S.,
1330 Dollner, M., Elkins, J. W., Fiore, A. M., Flynn, C. M., Guo, H., Hall, S. R., Hannun, R. A., Hills,
1331 A., Hintsa, E. J., Hodzic, A., Hornbrook, R. S., Huey, L. G., Jimenez, J. L., Keeling, R. F., Kim,
1332 M. J., Kupc, A., Lacey, F., Lait, L. R., Lamarque, J.-F., Liu, J., McKain, K., Meinardi, S., Miller,
1333 D. O., Montzka, S. A., Moore, F. L., Morgan, E. J., Murphy, D. M., Murray, L. T., Nault, B. A.,
1334 Neuman, J. A., Nguyen, L., Gonzalez, Y., Rollins, A., Rosenlof, K., Sargent, M., Schill, G.,
1335 Schwarz, J. P., Clair, J. M. S., Steenrod, S. D., Stephens, B. B., Strahan, S. E., Strode, S. A.,
1336 Sweeney, C., Thames, A. B., Ullmann, K., Wagner, N., Weber, R., Weinzierl, B., Wennberg, P.

1337   O., Williamson, C. J., Wolfe, G. M., and Zeng, L.: The NASA Atmospheric Tomography
1338   (ATom) Mission: Imaging the Chemistry of the Global Atmosphere, Bull. Am. Meteorol., 103,
1339   E761-E790, https://doi.org/10.1175/BAMS-D-20-0315.1, 2022.
1340
1341   Tilmes, S., Lamarque, J. F., Emmons, L. K., Kinnison, D. E., Ma, P. L., Liu, X., Ghan, S.,
1342   Bardeen, C., Arnold, S., Deeter, M., Vitt, F., Ryerson, T., Elkins, J. W., Moore, F., Spackman, J.
1343   R., and Val Martin, M.: Description and evaluation of tropospheric chemistry and aerosols in the
1344   Community Earth System Model (CESM1.2), Geosci. Model Dev., 8, 1395-1426, 10.5194/gmd-
1345   8-1395-2015, 2015.
1346
1347   Tilmes, S., Lamarque, J. F., Emmons, L. K., Kinnison, D. E., Marsh, D., Garcia, R. R., Smith, A.
1348   K., Neely, R. R., Conley, A., Vitt, F., Val Martin, M., Tanimoto, H., Simpson, I., Blake, D. R.,
1349   and Blake, N.: Representation of the Community Earth System Model (CESM1) CAM4-chem
1350   within the Chemistry-Climate Model Initiative (CCMI), Geosci. Model Dev., 9, 1853-1890,
1351   https://doi.org/10.5194/gmd-9-1853-2016, 2016.
1352
1353   USEPA: Guidance for Data Quality Assessment, Practical Methods for Data Analysis, Office of
1354   Environmental Information Washington, EPA QA/G-9, QA00 Update,
1355   https://www.epa.gov/sites/default/files/2015-06/documents/g9-final.pdf, 2000.
1356
1357   van Herpen, M. M. J. W., Li, Q., Saiz-Lopez, A., Liisberg, J. B., Röckmann, T., Cuevas, C. A.,
1358   Fernandez, R. P., Mak, J. E., Mahowald, N. M., Hess, P., Meidan, D., Stuut, J.-B. W., and
1359   Johnson, M. S.: Photocatalytic chlorine atom production on mineral dust–sea spray aerosols over
1360   the North Atlantic, Proceedings of the National Academy of Sciences, 120, e2303974120,
1361   10.1073/pnas.2303974120, 2023.
1362
1363   Wang, S., Kinnison, D., Montzka, S. A., Apel, E. C., Hornbrook, R. S., Hills, A. J., Blake, D. R.,
1364   Barletta, B., Meinardi, S., Sweeney, C., Moore, F., Long, M., Saiz-Lopez, A., Fernandez, R. P.,
1365   Tilmes, S., Emmons, L. K., and Lamarque, J.-F.: Ocean Biogeochemistry Control on the Marine
1366   Emissions of Brominated Very Short-Lived Ozone-Depleting Substances: A Machine-Learning
1367   Approach, J. Geophys. Res. Atmos., 124, 12319-12339, https://doi.org/10.1029/2019JD031288,
1368   2019a.
1369
1370   Wang, S., Apel, E. C., Schwantes, R. H., Bates, K. H., Jacob, D. J., Fischer, E. V., Hornbrook, R.
1371   S., Hills, A. J., Emmons, L. K., Pan, L. L., Honomichl, S., Tilmes, S., Lamarque, J.-F., Yang, M.,
1372   Marandino, C. A., Saltzman, E. S., de Bruyn, W., Kameyama, S., Tanimoto, H., Omori, Y., Hall,
1373   S. R., Ullmann, K., Ryerson, T. B., Thompson, C. R., Peischl, J., Daube, B. C., Commane, R.,
1374   McKain, K., Sweeney, C., Thames, A. B., Miller, D. O., Brune, W. H., Diskin, G. S., DiGangi, J.
1375   P., and Wofsy, S. C.: Global Atmospheric Budget of Acetone: Air-Sea Exchange and the
1376   Contribution to Hydroxyl Radicals, J. Geophys. Res. Atmos., 125, e2020JD032553,
1377   https://doi.org/10.1029/2020JD032553, 2020.
1378
1379   Wang, X., Jacob, D. J., Eastham, S. D., Sulprizio, M. P., Zhu, L., Chen, Q., Alexander, B.,
1380   Sherwen, T., Evans, M. J., Lee, B. H., Haskins, J. D., Lopez-Hilfiker, F. D., Thornton, J. A.,
1381   Huey, G. L., and Liao, H.: The role of chlorine in global tropospheric chemistry, Atmos. Chem.
1382   Phys., 19, 3981-4003, https://doi.org/10.5194/acp-19-3981-2019, 2019b.

1383
1384 Wang, X., Jacob, D. J., Downs, W., Zhai, S., Zhu, L., Shah, V., Holmes, C. D., Sherwen, T.,
1385 Alexander, B., Evans, M. J., Eastham, S. D., Neuman, J. A., Veres, P. R., Koenig, T. K.,
1386 Volkamer, R., Huey, L. G., Bannan, T. J., Percival, C. J., Lee, B. H., and Thornton, J. A.: Global
1387 tropospheric halogen (Cl, Br, I) chemistry and its impact on oxidants, Atmos. Chem. Phys., 21,
1388 13973-13996, https://doi.org/10.5194/acp-21-13973-2021, 2021.
1389
1390 Wiedinmyer, C., Kimura, Y., McDonald-Buller, E. C., Emmons, L. K., Buchholz, R. R., Tang,
1391 W., Seto, K., Joseph, M. B., Barsanti, K. C., Carlton, A. G., and Yokelson, R.: The Fire
1392 Inventory from NCAR version 2.5: an updated global fire emissions model for climate and
1393 chemistry applications, EGUsphere, 2023, 1-45, 10.5194/egusphere-2023-124, 2023.
1394
1395 Wiedmann, T. O., Guethner, B., Class, T. J., and Ballschmiter, K.: Global Distribution of
1396 Tetrachloroethene in the Troposphere: Measurements and Modeling, Environmental Science &
1397 Technology, 28, 2321-2329, 10.1021/es00062a016, 1994.
1398
1399 Wofsy, S. C., Afshar, S., Allen, H. M., Apel, E. C., Asher, E. C., Barletta, B., Bent, J., Bian, H.,
1400 Biggs, B. C., Blake, D. R., Blake, N., Bourgeois, I., Brock, C. A., Brune, W. H., Budney, J. W.,
1401 Bui, T. P., Butler, A., Campuzano-Jost, P., Chang, C. S., Chin, M., Commane, R., Correa, G.,
1402 Crounse, J. D., Cullis, P. D., Daube, B. C., Day, D. A., Dean-Day, J. M., Dibb, J. E., DiGangi, J.
1403 P., Diskin, G. S., Dollner, M., Elkins, J. W., Erdesz, F., Fiore, A. M., Flynn, C. M., Froyd, K. D.,
1404 Gesler, D. W., Hall, S. R., Hanisco, T. F., Hannun, R. A., Hills, A. J., Hintsa, E. J., Hoffman, A.,
1405 Hornbrook, R. S., Huey, L. G., Hughes, S., Jimenez, J. L., Johnson, B. J., Katich, J. M., Keeling,
1406 R. F., Kim, M. J., Kupc, A., Lait, L. R., McKain, K., McLaughlin, R. J., Meinardi, S., Miller, D.
1407 O., Montzka, S. A., Moore, F. L., Morgan, E. J., Murphy, D. M., Murray, L. T., Nault, B. A.,
1408 Neuman, J. A., Newman, P. A., Nicely, J. M., Pan, X., Paplawsky, W., Peischl, J., Prather, M. J.,
1409 Price, D. J., Ray, E. A., Reeves, J. M., Richardson, M., Rollins, A. W., Rosenlof, K. H., Ryerson,
1410 T. B., Scheuer, E., Schill, G. P., Schroder, J. C., Schwarz, J. P., St.Clair, J. M., Steenrod, S. D.,
1411 Stephens, B. B., Strode, S. A., Sweeney, C., Tanner, D., Teng, A. P., Thames, A. B., Thompson,
1412 C. R., Ullmann, K., Veres, P. R., Wagner, N. L., Watt, A., Weber, R., Weinzierl, B. B.,
1413 Wennberg, P. O., Williamson, C. J., Wilson, J. C., Wolfe, G. M., Woods, C. T., Zeng, L. H., and
1414 Vieznor, N.: ATom: Merged Atmospheric Chemistry, Trace Gases, and Aerosols, Version 2,
1415 Journal, Volume, Pages, https://doi.org/10.3334/ORNLDAAC/1925, 2021. access: 23 October
1416 2023,
1417
1418 Worton, D. R., Sturges, W. T., Schwander, J., Mulvaney, R., Barnola, J. M., and Chappellaz, J.:
1419 20th century trends and budget implications of chloroform and related tri-and dihalomethanes
1420 inferred from firn air, Atmos. Chem. Phys., 6, 2847-2863, https://doi.org/10.5194/acp-6-2847-
1421 2006, 2006.
1422

1423　SI:

1424　**Figure S1 Annual mean (2017) emissions of CH_2Cl_2 and contribution of different tagged**
1425　**source regions. AS: Asia, EU: Europe, NA: North America, SA: South America, AF:**
1426　**Africa, and ROW: Rest of the world.**

1427　**Figure S2 Vertical profiles of median CH_2Cl_2 mixing ratios measured during individual**
1428　**ATom deployments (columns) based on NCAR TOGA (black), UCI WAS (gold), and**
1429　**NOAA PFP (green) instruments over five different bins, accompanied by the CESM1**
1430　**modeling results (blue line). Also, NCAR TOGA measurements during ORCAS (green)**
1431　**and CONSTRAST (cyan) missions are shown. All individual data points are shown only for**
1432　**TOGA instrument (only up to the upper limit of X-axis).**

1433　**Figure S3 Same as Figure S3 for C_2Cl_4.**

1434　**Figure S4 Same as Figure S3 for $CHCl_3$.**

1435　**Figure S5 Vertical profiles of median 1,2-DCA mixing ratios measured during Atom-4**
1436　**deployments based on NCAR TOGA (black), UCI WAS (gold), and NOAA PFP (green)**
1437　**instruments over five different bins, accompanied by the CESM1 modeling results (blue**
1438　**line). All individual data points are shown only for TOGA instrument (only up to the upper**
1439　**limit of X-axis).**

1440　**Figure S6 Scatter plots of different Cl-VSLS measured by NCAR TOGA instrument**
1441　**during a,d) CONTRAST missions, b,e) ORCAS mission, and c,f) Atom-2 deployment color**
1442　**coded by latitude bins. Note that axis limits are different in each panel.**

1443　**Figure S7 Spatial binned distribution of mean modeled (top subplot) and measured**
1444　**(bottom subplot) for $CHCl_3$ (a-d) and OH (e-h) mixing ratios during individual ATom**
1445　**missions. Latitude and altitude bin intervals are 5 degrees and 1km, respectively. Note that**
1446　**the measured OH data are based on ATHOS instrument.**

1447　**Figure S8 Vertical profile contribution (percentage) of CH_2Cl_2 tagged emissions during**
1448　**each individual ATom deployment over the Pacific and Atlantic sides. Percentages are**
1449　**normalized values for each panel. AS: Asia, EU: Europe, NA: North America, SA: South**
1450　**America, AF: Africa, and ROW: Rest of the world.**

1451　**Figure S9 Same as Figure S9 for C_2Cl_4.**

1452　**Figure S10** Vertical profiles of median CH_2Cl_2, C_2Cl_4, and $CHCl_3$ mixing ratios measured
1453　during all ATom missions based on NCAR TOGA (black), base model (blue line), and base
1454　model with 10% reduction for OH reaction constant of Cl-VSLS(red line) over five different
1455　bins. The OH reaction constant is reduced by 10% for R2, R5, and R8 to compensate for the
1456　model high OH abundance.

1457　**Figure S11 Annual zonal mean (2016-2018) of Cl atom, Cl_2 molecule, and HOCl.**

1458　**Figure S12 Spatial binned distribution of mean modeled (top subplot) and measured**
1459　**(bottom subplot) for Cl_2 during Atom-3 and Atom-4 deployments. Latitude and altitude**

1460 **bin intervals are 5 degrees and 1km, respectively. Note that the measured data are based**
1461 **on NOAA CIMS instrument**

1462 **Figure S13 Zonal seasonal mean (2016-2018) local lifetime (days) of a-d) CH$_2$Cl$_2$, e-h)**
1463 **C$_2$Cl$_4$. The solid line shows the mean tropopause.**

1464 **Table S1 Number of TOGA data used for each compound from ATom mission. LOD:**
1465 **Limit of Detection, NaN: Not a Number.**

1466 **Table S2 Monthly mean (106-2018) model evaluation results against ground measurement**
1467 **sites.**

1468 **Table S3** *Summary of the Cl-VSLS data, over tropical upper troposphere, measured by TOGA*

1469 **Table S4 Model evaluation results for CH$_2$Cl$_2$ against the ATom deployments.**

1470 **Table S5 Model evaluation results for C$_2$Cl$_4$ against the ATom deployments.**

1471 **Table S6 Model evaluation results for CHCl$_3$ against the ATom deployments.**

1472 **Table S7 Model evaluation results for 1,2-DCA against ATom-4 deployment.**

1473

1489 **Figure 3** Vertical profiles of the median Pacific minus median Atlantic mixing ratios for (a)
1490 CH$_2$Cl$_2$, (b) C$_2$Cl$_4$, and (c) CHCl$_3$ from the TOGA observations at northern mid-latitudes (20–

1534

1535